Accepted Manuscript

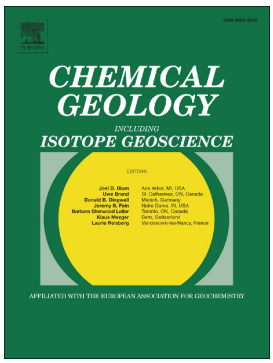

Multiple sulphur isotope records tracking basinal and global processes in the 1.98 Ga Zaonega Formation, NW Russia

K. Paiste, A. Lepland, A.L. Zerkle, K. Kirsimäe, G. Izon, N.K. Patel, F. McLean, T. Kreitsmann, K. Mänd, T.H. Bui, A.E. Romashkin, D.V. Rychanchik, A.R. Prave

PII: S0009-2541(18)30465-0
DOI: doi:10.1016/j.chemgeo.2018.09.025
Reference: CHEMGE 18918

To appear in: *Chemical Geology*

Received date: 13 May 2018
Revised date: 14 September 2018
Accepted date: 16 September 2018

Please cite this article as: K. Paiste, A. Lepland, A.L. Zerkle, K. Kirsimäe, G. Izon, N.K. Patel, F. McLean, T. Kreitsmann, K. Mänd, T.H. Bui, A.E. Romashkin, D.V. Rychanchik, A.R. Prave , Multiple sulphur isotope records tracking basinal and global processes in the 1.98 Ga Zaonega Formation, NW Russia. Chemge (2018), doi:10.1016/j.chemgeo.2018.09.025

Multiple sulphur isotope records tracking basinal and global processes in the 1.98 Ga Zaonega Formation, NW Russia

K. Paiste[a,*], A. Lepland[a,b,d], A. L. Zerkle[c], K. Kirsimäe[d], G. Izon[c,1], N. K. Patel[c], F. McLean[c], T. Kreitsmann[d], K. Mänd[d,f], T. H. Bui[e], A. E. Romashkin[g], D. V. Rychanchik[g], A. R. Prave[c]

[a]CAGE—Centre for Arctic Gas Hydrate, Environment and Climate, Department of Geosciences, UiT The Arctic University of Norway, 9037 Tromsø, Norway.

[b]Geological Survey of Norway (NGU), 7491 Trondheim, Norway.

[c]School of Earth and Environmental Sciences and Centre for Exoplanet Science, University of St Andrews, St Andrews, KY16 9AL Scotland/UK.

[d]Department of Geology, University of Tartu, 50411 Tartu, Estonia.

[e]Department of Earth & Planetary Sciences, McGill University, 3450 University Street Montreal, Quebec, Canada H3A 0E8.

[f]Department of Earth & Atmospheric Sciences, University of Alberta, Edmonton, Alberta T6G 2E3, Canada.

[g]Institute of Geology, Karelian Science Centre, Pushkinskaya 11, 185610 Petrozavodsk, Russia.

*Corresponding author: email kart.paiste@gmail.com, phone +372 55694372

[1]Present address: Department of Earth, Atmospheric and Planetary Sciences, Massachusetts Institute of Technology, E25-631: 45 Carleton Street, Cambridge, MA 02142, USA.

Abstract

The exceptionally organic-rich rocks of the 1.98 Ga Zaonega Formation deposited in the Onega Basin, NW Russia, have refined our understanding of Earth System evolution during the Paleoproterozoic rise in atmospheric oxygen. These rocks were formed in vent- or seep-influenced settings contemporaneous with voluminous mafic volcanism and contain strongly ^{13}C-depleted organic matter. Here we report new isotopic ($\delta^{34}S$, $\Delta^{33}S$, $\Delta^{36}S$, $\delta^{13}C_{org}$) and mineralogical, major element, total sulphur and organic carbon data for the upper part of the Zaonega Formation, which was deposited shortly after the termination of the Lomagundi-Jatuli positive carbon isotope excursion. The data were collected on a recently obtained 102 m drill-core section and show a $\delta^{13}C_{org}$ shift from -38‰ to -25‰. Sedimentary sulphides have $\delta^{34}S$ values typically between +15‰ and +25‰ reflecting closed-system sulphur isotope behaviour

driven by high rates of microbial sulphate reduction, high sulphate demand, hydrothermal activity and hydrocarbon seepage. Four intervals record $\delta^{34}S$ values that exceed +30‰. We interpret these unusually ^{34}S-enriched sulphides to be a result of limited sulfate diffusion into pore waters due to changes in sedimentation and/or periods of basinal restriction. Additionally, there are four negative $\delta^{34}S$ and positive $\Delta^{33}S$ excursions that are interpreted to reflect changes in the open/closed-system behaviour of sulphate reduction or availability of reactive iron. Our findings highlight the influence of basinal processes in regulating sulphur isotope records and the need for care before interpreting such signals as reflecting global conditions.

Keywords: Paleoproterozoic, Zaonega Formation, sulphur cycle, carbon cycle, Great Oxidation Event

1. Introduction

The Paleoproterozoic represents a period in Earth's history, when a series of (bio)geological events ultimately led to a change in the redox state of Earth's atmosphere-ocean system and the rise of atmospheric oxygen at ca. 2.3 Ga during the Great Oxidation Event (GOE; Bekker et al., 2004; Holland, 2006; Guo et al., 2009; Luo et al., 2016; Gumsley et al., 2017; but see also Ohmoto et al., 2014). Following the GOE, the carbon cycle experienced unprecedented perturbations, featuring the large-magnitude Lomagundi-Jatuli positive carbonate carbon isotope excursion between 2.2 and 2.06 Ga (Karhu and Holland, 1996; Martin et al., 2013) and the subsequent accumulation of organic-rich sediments during the ca. 2.0 Ga Shunga Event (Melezhik et al., 1999, 2004; Strauss et al., 2013). It is postulated that these carbon cycle perturbations were driven by intensified subaerial oxidative weathering, with concomitant increases in riverine-derived nutrients, intensifying biological activity and facilitating the growth of the marine sulphate reservoir (Bekker et al., 2006; Schröder et al., 2008; Reuschel et al., 2012). Such inferences are supported by the presence of the oldest known globally significant phosphorites associated with the Shunga Event (Bekker et al., 2003; Lepland et al., 2013, 2014) and the oldest extensive evaporites of the ca. 2.0 Ga Tulomozero Formation, which also archive the Lomagundi-Jatuli excursion in the Onega Basin of NW Russia (Morozov et al., 2010; Krupenik et al., 2011; Blättler et al., 2018). Geochemical modelling of the evaporite mineralogy and calcium isotope systematics of the latter indicate that, by ca. 2.0 Ga, the concentration of seawater sulphate (SWS) was sufficiently high (>10 mM) to allow precipitation of marine evaporite sequences with gypsum/anhydrite, halite and bittern salts (Blättler et al., 2018). Such global-scale changes would seem to signify an irreversible trajectory

in Earth's redox state following the GOE. However, pyrite-derived sulphur isotope data obtained from the organic-rich rocks of the 1.98 Ga Zaonega Formation and ca. 2.1 Ga Francevillian Group have been used to argue for an environmental change and contraction of the SWS reservoir (Scott et al., 2014; Ossa-Ossa et al., 2018). This conclusion was reached by combining iron-speciation results with multiple-sulphur isotope data, interpreted to reflect development of euxinic conditions on two different cratons with highly positive pyrite $\delta^{34}S$ values coupled to opposing $\Delta^{33}S$-$\delta^{34}S$ behaviour suggesting low sulphate concentrations (Scott et al., 2014; Ossa-Ossa et al., 2018).

To assess the significance of the carbon- and sulphur-isotope signals archived in the Zaonega Formation against the backdrop of Earth System change, we have undertaken a multi-proxy geochemical and petrographic study using recently obtained drill core material from the upper part of the Formation (Fig.1). Samples were taken at approximately one metre intervals through a 102-m thick section drilled in 2012 in the upper part of the Formation. Our multi-proxy dataset extends the stratigraphic coverage of the isotopic profiles reported in previous studies to better characterise the physical and chemical conditions under which biogeochemical carbon and sulphur cycling occurred at ca. 2.0 Ga.

2. Geological background

The Zaonega Formation forms the upper part of the Paleoproterozoic succession of the Onega Basin (Melezhik et al., 2013b) in the Karelia region of NW Russia (Fig. 1a). The succession consists of mostly greenschist facies volcano-sedimentary rocks that lie unconformably on Archean granites and gneisses. The entire succession was deformed into a series of open folds cut by high-angle faults during the 1.89–1.79 Ga Svecofennian orogeny (Melezhik et al., 1999; Ojakangas et al., 2001). The 1500 m thick Zaonega Formation occurs above the ^{13}C-enriched shallow-marine carbonate rocks of the Tulomozero Formation and is overlain by basalts of the Suisari Formation (Melezhik et al., 1999; Črne et al., 2013b). The proposed depositional model for the Zaonega Formation suggests accumulation in a rift basin marked by contemporaneous shallow-and deep-water mixed siliciclastic-carbonate deposition (Črne et al., 2014; Melezhik et al., 2015).

The Zaonega Formation is younger than the Lomagundi-Jatuli event which terminated in Fennoscandia at 2.06 Ga (Karhu and Holland, 1996; Melezhik et al., 1999, 2004) and is older than a suite of cross-cutting dykes that yield ages of 1919 ± 18 Ma (Priyatkina et al., 2014),

1956 ± 5 Ma (Stepanova et al., 2014) and 1961.6 ± 5.1 Ma (Martin et al., 2015); it also predates the gabbro sills in the overlying Suisari Formation dated at 1969 ± 18 Ma (Puchtel et al., 1998) and 1988 ± 34 Ma (Puchtel et al., 1999). Hence the age of the Zaonega Formation has been previously constrained to a time interval between 2.06 and 1.98 Ga. More recently, Martin et al. (2015) place deposition between 1975.3 ± 2.8 Ma and 1967.6 ± 3.5 Ma, but these constraints require additional assessment. In the absence of an agreed upon precise depositional age, we adopt a 1.98 Ga estimate for the age of the Zaonega Formation.

The Zaonega Formation features well-preserved organic- and phosphorous-rich siliciclastic and carbonate rocks with organic carbon contents reaching 40% in the mudstone units and up to 90% in pyrobitumen-filled veins (Melezhik et al., 1999, 2004, 2013a). Graded greywackes interbedded with mudstones, dolostones and limestones have been interpreted as turbidity-current deposits, punctuating background hemipelagic sedimentation. Deposition occurred alongside syndepositional mafic magmatism in the form of mafic tuffs, lavas and gabbroic sills. Peperitic contacts between the igneous and enclosing sedimentary rock indicate emplacement into wet and unconsolidated sediments (Galdobina, 1987; Črne et al., 2013a, b; Melezhik et al., 2015). Heat provided by this igneous activity triggered hydrothermal circulation and oil generation as the organic-rich rocks passed through the oil window (Qu et al., 2012; Črne et al., 2013a, b).

A comprehensive $\delta^{13}C_{org}$ dataset was previously obtained from FAR-DEEP cores 12AB and 13A that intersect 550 m of the Zaonega Formation. These data reveal a decline in $\delta^{13}C_{org}$ values from -25‰ to -40‰ in the middle–upper Zaonega Formation prior to a return to values of -25‰ (Kump et al., 2011; Qu et al., 2012; Lepland et al., 2014). Abundant sulphide minerals associated with the organic-rich rocks have variable $\delta^{34}S$ values ranging from -19‰ to +27‰ (Shatsky, 1990, Scott et al., 2014), but generally become more ^{34}S-enriched up-section with typical values of ~+15‰ in $\delta^{34}S$ (Scott et al., 2014). Several contrasting explanations have been proposed to explain these isotopic trends, including global-scale oxidation of organic matter (Kump et al., 2011), seepage/spillage of locally generated hydrocarbons to the seafloor triggering basinal methanotrophy (Qu et al., 2012), and a biogeochemical response to a global collapse of the SWS reservoir (Scott et al., 2014). The first scenario is questionable since the initial negative $\delta^{13}C_{org}$ excursion coincides with the Lomagundi-Jatuli positive excursion in $\delta^{13}C_{carb}$ (Ossa-Ossa et al., 2018) and both excursions cannot be explained by a single, global underlying cause. Even though hydrocarbon migration and seepage are considered as the main factors in governing the negative $\delta^{13}C_{org}$ shift in the Zaonega Formation, Qu et al. (2012) related

this to a local bloom of methanotrophic organisms that induced high rates of pore water sulphate reduction, while Scott et al. (2014) proposed that the negative co-variation of $\delta^{34}S$ and $\delta^{13}C_{org}$ values signalled water column methanotrophy and an overall increase in methane production as a response to low sulphate concentrations. Considering such contrasting scenarios, the need to discriminate between global, basinal and post-depositional controls becomes evident.

2.1 Sulphur isotope systematics

Geochemical and biological processes fractionate sulphur isotopes to different extents. The largest known non-photochemical sulphur isotope fractionations are associated with reduction, and to a lesser extent oxidation, reactions mediated by microbial communities (Johnston et al., 2011). Microbial sulphate reduction (MSR) coupled to oxidation of organic matter is the dominant pathway for anaerobic respiration in contemporary sediments. In Phanerozoic marine environments with high SWS concentrations, precipitation and burial of sulphide minerals (ultimately pyrite), mediated by MSR, is the main sink for sulphide. When sulphate concentrations exceed 0.2 mM (Habicht et al., 2002; Bradley et al., 2016) the kinetic isotope effect associated with MSR becomes pronounced, depleting the sulphate pool in ^{32}S via its preferential incorporation into the sulphide product. Owing to MSR, modern seawater has a $\delta^{34}S$ value of 21‰, and the sulphide product (and resulting pyrite sink) can be depleted in ^{34}S (Rees et al., 1978; Seal, 2006; Canfield et al., 2010) by as much as 70‰ based on experimental studies (Sim et al., 2011), although fractionations between 20‰ to 60‰ are common in nature (Zaback et al., 1993). In sediments where sulphate demand exceeds sulphate supply, the sulphur isotope composition of product sulphides will approach that of the sulphate (Goldhaber and Kaplan, 1975; Jørgensen, 1979). The final $\delta^{34}S$ of sulphide that is preserved in the rock record primarily as pyrite will also depend on multiple factors including iron availability and organic carbon loading (Zaback et al., 1993; Aller et al., 2010; Fike et al., 2015). If the ambient sulphate reservoir is limiting then ongoing MSR will deplete the residual sulphate in ^{32}S and generate parallel increases in local $\delta^{34}S_{SWS}$ and $\delta^{34}S_{pyr}$, with similar effects registered in the minor sulphur isotope ratios ($\delta^{33}S$ and $\delta^{36}S$; Johnston et al., 2008, 2007; Gomes and Hurtgen, 2013; Fike et al., 2015). Further, S-based chemoautotrophic metabolisms also impart a small but distinguishable $\delta^{34}S$ fractionation, expressed when sulphide and other reduced sulphur compounds are oxidised to elemental sulphur and sulphate (Balci et al., 2007; Zerkle et al., 2009, 2016). Additionally, microbial sulphur disproportionation (MSD) uses intermediate redox state sulphur species to produce both sulphate and sulphide, causing additional $\delta^{34}S$

fractionations of up to 20‰ (Canfield and Thamdrup, 1994; Farquhar et al., 2003; Johnston et al., 2005a).

All these various sulphur-utilising metabolisms have the capacity to produce overlapping $\delta^{34}S$ signatures, making it difficult to identify unambiguously specific metabolic pathways from $\delta^{34}S$ values preserved in the rock record. Furthermore, the extent of fractionation during MSR depends on many factors such as cell-specific sulphate reduction rates, temperature, electron donor availability, sulphate concentration, salinity and pH (Fike et al., 2015). Moreover, pure culture experiments are rarely representative of natural environments where S-cycling consortia often do not produce unique $\delta^{34}S$ isotope signatures (Detmers et al., 2001; Brüchert, 2004; Johnston et al., 2011; Sim et al., 2011). Recent studies, however, have demonstrated that biogeochemical sulphur cycling can cause mass-dependent fractionations that affect the partitioning of sulphur's minor isotopes (Johnston et al., 2005a, 2011; Seal, 2006; Canfield et al., 2010; Zerkle et al., 2016). These small differences are resolvable in the minor sulphur isotopes ratios and can provide additional information even when $\delta^{34}S$ values overlap.

3. Methods

3.1 Materials

Samples were collected from two 60-m long cores that were drilled 500 m apart: OnZap1 (62.5870 N, 34.9310 E) and OnZap3 (62.5920 N, 34.9280 E) near the village of Shunga in Karelia, NW Russia (Fig. 1). A third core, OnZap2, was drilled 70 m from OnZap1 and was used for additional sedimentological and petrographic description. Between OnZap1 and OnZap3 is the site of the 240-m long FAR-DEEP 13A core. A distinct dolomite-chert unit occurs in each of the OnZap and FAR-DEEP cores (Črne et al., 2014), and its base is used as a lithostratigraphic marker to enable correlations between cores. The overlapping OnZap cores, therefore, provide a 102-m thick section of the upper Zaonega Formation, which we term the OnZap section. Unless otherwise stated, all depths discussed hereafter refer to the composite OnZap section (see the supplementary Tables for individual core depths and thicknesses). Detailed lithological logging of the cores was performed prior to sampling. Sample locations were carefully selected to minimise the effects of secondary overprints (e.g. large concretions, veins, fractures). In total 134 samples were obtained at approximately 1 metre intervals through cores OnZap1 and OnZap3 to produce our chemostratigraphic data set.

3.2 Petrographical, mineralogical and major element analyses

Petrographic characterisation of thin sections was performed by scanning electron microscope (SEM) analysis using a ZEISS EVO MA15 SEM at the University of Tartu. The images were captured in backscattered electron (BSE) mode. To complement the SEM imaging, chemical characterisation by point analyses and elemental mapping of the samples were performed using an Oxford AZTEC-MAX energy-dispersive spectrometer (EDS).

Major element composition was determined by Bureau Veritas Minerals, Vancouver, Canada by inductively coupled plasma optical emission spectroscopy (ICP-OES). Powdered samples were fused at 950 °C with lithium metaborate flux and the fusion beads were digested with a combination of hydrofluoric and perchloric acids prior to analysis. Loss on ignition data were obtained from heating samples in a furnace at 950 °C for 1 h. For all elements, average percent relative standard deviation (average RSD%) was less than 5%. The mineralogical composition of whole rock samples was determined on unoriented powdered samples using a Bruker D8 Advance X-ray diffractometer using Cu Kα radiation and LynxEye positive sensitive detector in 2–70° 2-Theta range at the University of Tartu. The obtained diffractograms were interpreted and modelled with the Rietveld algorithm-based program Topaz. The content of crystalline phases determined by XRD analysis were normalised to account for X-ray amorphous organic carbon using the TOC abundance data determined from the same samples.

3.3 Sulphur and carbon content

The total carbon (TC), total organic carbon (TOC) and total sulphur (TS) abundances were quantified using ~100 mg aliquots of powdered sample admitted to a LECO SC-444 analyser at the Geological Survey of Norway. The TOC content was determined on acid-treated (10% HCl vol/vol) residues. Detection limits for TS, TC and TOC were 0.02 wt.%, 0.06 wt.% and 0.1 wt.%, respectively. The relative precision was better than 2.5% for TC and 10% for TS and TOC.

3.4 Sulphur isotope analyses

Powdered samples were subjected to a two-step sulphur extraction procedure (Canfield et al., 1986). In this sequential extraction method, sulphur is liberated first as H_2S from acid volatile sulphur (AVS; monosulphides such as pyrrhotite, sphalerite, mackinawite or greigite) via a 6 M HCl distillation, and pyrite is released via hot chromium(II) chloride distillation (CRS). To prevent incorporation of elemental sulphur to the CRS fraction, we used chromium(II) chloride solution adopted from Oduro et al. (2013). In addition to pyrite, the CRS solution may have

attacked marcasite, however our XRD analysis failed to detect this pyrite polymorph, rendering any potential contribution negligible. The resulting H_2S was converted into Ag_2S by adding of 0.1 M $AgNO_3$. The precipitate was then cleaned using 1M $NH_4(OH)$ and rinsed to neutrality using ultra-pure (18 MΩ·cm) water (Oduro et al., 2013).

Sulphur isotope analyses were performed at McGill University. The Ag_2S samples were reacted overnight with excess fluorine gas in nickel bombs at 250 °C to produce SF_6 that was first purified cryogenically and then via gas chromatography. The sulphur isotope composition of purified SF_6 was measured by dual-inlet gas-source mass spectrometry monitoring ion beams at m/z of 127, 128, 129, and 131 using a Thermo Finnigan MAT 253 gas source mass spectrometer. Sample reproducibility, as determined by replicate analyses of the in-house standard MSS-1, was generally better than 0.1‰ for $\delta^{34}S$ values, 0.015‰ for $\Delta^{33}S$ and 0.2‰ for $\Delta^{36}S$. Sulphur isotope ratios are reported in the standard delta notation as *per mil* deviations from the international reference standard the Vienna-Canyon Diablo Troilite (V-CDT):

$$\delta^{3x}S = 1000 \cdot ({}^{3x}R_{sample}/{}^{3x}R_{V\text{-}CDT} - 1),$$

where ${}^{3x}R = {}^{3x}S/{}^{32}S$, for 3x = 33, 34 or 36.

We express the minor isotope values in capital delta notation:

$$\Delta^{33}S = \delta^{33}S - 1000 \cdot [(1 + \delta^{34}S/1000)^{0.515} - 1],$$

and

$$\Delta^{36}S = \delta^{36}S - 1000 \cdot [(1 + \delta^{34}S/1000)^{1.9} - 1].$$

3.5 Organic carbon isotope analyses

Between 0.2 and 2 g aliquots of homogenised sample powders were reacted with 10% (vol/vol) HCl at room temperature in centrifuge tubes for 24 hours. Acid treatment was repeated until no further reaction was observed. The remaining residues were rinsed to neutrality using deionised water and dried at 45 ºC. Aliquots of dry decarbonated residue (0.2 mg) were then weighed into tin capsules and the organic carbon isotope ($\delta^{13}C_{org}$) composition was determined by flash combustion using an Elemental Analyser coupled to a Continuous Flow Isotope Ratio Mass Spectrometer (ThermoScientific Delta V Plus with Costech EA) at the NERC Life Sciences Mass Spectrometry Facility at the Scottish Universities Environmental Research Centre in East Kilbride, Scotland.

The carbon isotope results are reported in standard delta notation as *per mil* deviation from the Vienna-Pee Dee Belemnite (V-PDB) standard:

$\delta^{13}C = 1000 \cdot (^{13}R_{organic\text{-}C}/^{13}R_{V\text{-}PDB} - 1)$.

Accuracy and precision was monitored via replicate analyses of the international standard USGS40 L-glutamic acid ($\delta^{13}C$= –26.39 ± 0.04‰ V-PDB), which yielded an average $\delta^{13}C$ value of –26.19 ± 0.04‰. The $\delta^{13}C$ values have been corrected for the 0.2‰ offset between the measured and expected values of USGS40 measurements.

4. Results

4.1 Lithology and mineralogy

Characteristic rock types and lithostratigraphic columns together with selected mineralogical and geochemical parameters are presented in Figures 2 to 6. All mineralogical and geochemical results are provided in Supplementary Tables 1 to 4. Correlation between OnZap cores was made using the base of a massive dolomite interval that can be identified across the basin, occurring at 53 m in OnZap1 and at 10.8 m in OnZap3 (Figs. 4–6). The cores recovered organic-rich mudstone, dolostone and calcareous mudstone from the upper part of the Zaonega Formation (Fig. 2). The upper part of OnZap1 provides an additional 25 m of stratigraphy with respect to previous studies (Qu et al., 2012; Črne et al., 2013 a, b, 2014; Lepland et al., 2014; Scott et al., 2014). Three units can be identified: Unit A, from 102–53 m depth, composed of black organic-rich mudstones with a few carbonate beds; Unit B, from 53–33 m, consisting predominantly of dolostone beds including the massive dolomite interval; and Unit C, from 33–1.7 m, characterised by grey relatively organic-poor mudstone and marly carbonate beds (Figs. 2, 4).

4.1.1 Unit A: organic-rich mudstones (102–53 m depths)

Organic-rich mudstones display wispy, low-angle cross lamination and pass upward into calcareous mudstones marked by clay partings. The former contain quartz comprising up to 72 wt.%, mica at ~17 wt.%, variable amounts of K-feldspar up to ~24.6 wt.% and minor amounts of pyrite, calcite, talc and chlorite. The mica is predominantly a muscovite-type K-mica and a phlogopite-type Fe/Mg-mica with Fe/(Mg + Fe) ratios in the range of 0.03–0.04, hereafter referred to as Fe-poor Fe/Mg-mica. Pyrite abundances are relatively constant at 1–3 wt.% in the lower part of Unit A but are elevated (maximum of 13.8 wt.%) in organic-rich mudstones

in its upper part. Dolomite is the main carbonate mineral, but calcite reaches ~10 wt.% in some of the carbonate beds particularly along bed margins where it may co-occur with talc (also noted by Črne et al., 2014, in the FAR-DEEP cores). A few carbonate beds in the upper part of Unit A contain ~2 wt.% of an iron-rich dolomite to ankerite solid-solution phase, that can constitute up to 12.8 wt.%. The calcareous mudstone at 86–77 m contains up to 15.2 wt.% talc and 29.3 wt.% calcite, but also has low abundances of other minerals.

Cross-cutting veins are ubiquitous. Those in mudstones are predominantly filled with pyrobitumen, quartz and Fe-poor Fe/Mg-mica, whereas those in carbonate beds largely consist of calcite (Figs. 2d, e). The interval at 77–70 m depth displays intense veining and silicification at mudstone-dolostone contacts; here quartz can comprise up to 73.2 wt.% of the silicified intervals. The mudstones in this interval are finely laminated and exhibit soft-sediment deformation features that are cut by quartz veins (Fig. 2e).

Organic matter occurs as disseminated particles, pyrobitumen veins or as nodular aggregates (a few hundred μm in diameter) in finely laminated mudstone and calcareous mudstone. An organic-rich mudstone interval at 59–53 m depth has C_{org} contents of up to 65 wt.% and contains a thin layer at 54 m depth of bedding-parallel nodules composed of pyrobitumen and varying amounts of mica and pyrite. Its upper margin is marked by apatite nodules, layers and lenses.

4.1.2 Unit B: dolomite unit (53–33 m depths)

The dolostone interval defining the base of Unit B is cut by conspicuous black, massive chert veins that can be up to several meters thick and form an often bed-parallel network associated with thin mudstone interlayers. They contain relicts of the altered dolostone and their contacts with the dolostone layers are marked by calcite, Fe-poor Fe/Mg-mica and talc. Smaller, mm- to cm-scale veins are abundant and consist mainly of quartz, calcite, pyrobitumen and pyrite. The central parts of the dolostone beds are massive, nearly pure, dolomite that lacks pervasive silica veining and secondary calcite. The iron-rich dolomite to ankerite solid-solution phase is a common subcomponent (~6 wt.%) of the dolostone beds and increases in content up section, concomitant with a decrease in the frequency, extent and thickness of chert veining. In the upper part of Unit B dark grey mudstone beds become more numerous and are composed of quartz (~20 wt.%), mica (~40 wt.%; mainly muscovite-type K-mica but Fe-poor Fe/Mg-mica is also present) organic matter and K-feldspar (~2 wt.%, maximum of 11.4 wt.%). Pyrite is most abundant in the mudstones (~8 wt.%, maximum of 16.5 wt.%), but is also a common mineral component in the carbonate beds.

4.1.3 Unit C: relatively organic-poor rocks (33–1.7 m depths)

Unit C is composed of alternating fine-grained mudstone, calcareous mudstone and carbonate beds. The grey mudstones are finely parallel to ripple cross-laminated (Figs. 2a, c) and organic matter is lower than in Units A and B, with typical TOC values of ~1 wt.% but can be as high as 10 wt.%. Quartz and mica minerals comprise approximately ~35 wt.% and ~40 wt.%, respectively. The latter are muscovite-type K-mica and a biotite-type Fe/Mg-mica with Fe content ~20.8 wt.% (hereafter referred to as Fe-rich Fe/Mg-mica). Unlike the underlying units, the content of K-feldspar, Fe-poor Fe/Mg-mica and calcite is low and talc is absent. In contrast, plagioclase is more abundant reaching up to 13.2 wt.%. Overall, the content of disseminated pyrite in Unit C is lower than in Units A and B (~1.6 wt.%), although large pyrite aggregates and vein pyrite do occur. The iron-rich dolomite to ankerite solid-solution phase is a major mineral component of the marly carbonate beds of Unit C and its content increases upwards in the section reaching 38.5 wt.%. The marly carbonate beds vary from being massive with faint lamination in their centres to cross laminated with mud drapes (Fig. 2b). Siderite, in association with large anhedral pyrite, occurs in some of the marly carbonate beds and calcareous mudstones in the uppermost part of Unit C. Petrographically the siderite-pyrite aggregates occur as irregular to oval/lens-like masses of few hundred microns to few mm size. Siderite patches are to different extent replaced by pyrite aggregates composed of euhedral crystallites. Typically, the replacement of siderite aggregates starts at the contacts with the surrounding mudstone and progresses inwards.

4.1.4 Pyrite petrography

Core inspection and petrographic analyses show that sulphide minerals are pervasive but are typically concentrated within mudstone beds, with the highest abundances at the top of Unit A. Pyrite is the main sulphide mineral, but minor pyrrhotite, sphalerite, and As-, Cu- and Ni-bearing sulphides also occur. The minor sulphides are most abundant in Units A and B and mostly absent in Unit C. Most pyrite occurs as fine-grained euhedral and typically octahedral crystals ~10 μm in size (Figs. 3a, b, c). The central parts of individual pyrite crystals can be either hollow or contain inclusions of quartz, mica and rarely Cu-sulphide minerals. These minute pyrite crystals are concentrated in organic-rich layers within mudstones or carbonaceous mudstones and many occur as ellipsoidal, densely packed 30–100 μm sized clusters (Fig. 3a, b) encased within contorted mudstone layers.

Pyrite also occurs throughout the succession as large euhedral or anhedral disseminated crystals or irregular aggregates (Fig. 3d). The latter is most abundant in Units A and B and is associated

with other metal sulphides, such as sphalerite. Solitary large pyrite crystals (> 100 μm) are abundant in carbonate and calcareous mudstone beds but less so in mudstones. These large pyrite crystals commonly contain numerous inclusions of quartz and dolomite. At 27 m in Unit C, a dolostone bed contains large aggregates of pyrite that form clusters several cm in size with dolomite inclusions that appear texturally co-genetic with calcite (Fig. 3d).

4.2 Major element geochemistry

Stratigraphic profiles of selected major elements are reported as oxides and shown in Figure 5. Full datasets are in Supplementary Tables 1–4. The stratigraphic distribution of SiO_2, Al_2O_3 and K_2O show close correspondence with the mineral abundances of quartz, mica and feldspar, serving as a proxy for the respective mineral phases. The highest SiO_2 (~78 wt.%) and the lowest Al_2O_3 (~5 wt.%), Fe_2O_3* (~2 wt.%; total Fe expressed as Fe_2O_3) and K_2O (~2 wt.%) abundances are observed in the lower part of Unit A and in the dolostone interval at the base of Unit B (53–44 m). The SiO_2 content slightly decreases in the upper part of Unit B and in Unit C, whereas Al_2O_3 (~14 wt.%), Fe_2O_3* (~9 wt.%) and K_2O (~5 wt.%) abundances increase. Contents of TS and TOC vary from 0.02 wt.% to 10.9 wt.% and 0.12 wt.% to 65 wt.%, respectively. The highest TS and TOC abundances are observed in the upper parts of Units A and B with TS averaging ~2 wt.% (maximum of 10.9 wt.%) and TOC averaging ~13 wt.% (maximum of 65 wt.%). In Unit C, TS content has average values of ~1 wt.% (maximum of 4.3 wt.%) and TOC ~1 wt.% (maximum of 3.3 wt.%). The depth profiles of TS and Fe_2O_3* abundances co-vary in Units A and B, but are decoupled in Unit C where iron concentrations are the highest. This marked change in Fe_2O_3*, TOC and TS contents in Unit C coincides with an increase in Al_2O_3, a change in the mica phase from Fe-poor to Fe-rich Fe/Mg mica, increasingly more abundant Fe-rich carbonate phases, and a decrease in pyrite abundance.

4.3 Carbon isotope composition of organic matter

Organic carbon isotope ($\delta^{13}C_{org}$) values show an increase from -38.03‰ in Unit A to -24.51‰ in Unit C (Fig. 6). Unit B represents a transitional interval, with $\delta^{13}C_{org}$ values varying from -38‰ to -29‰. The same range of values and a similar shift in $\delta^{13}C_{org}$ was documented in FAR-DEEP 13A core by Lepland et al. (2014). As described below, this shift in $\delta^{13}C_{org}$ values is accompanied by a shift to more ^{34}S-enriched sulphides and lower TOC and TS concentrations.

4.4 Sulphur isotope composition of sulphides

Sulphur isotope data are shown in Figure 6 and the CRS and AVS data are reported in Supplementary Table 1. The $\delta^{34}S$, $\Delta^{33}S$ and $\Delta^{36}S$ values of the pyrite sulphur (CRS) in the

OnZap section range from -0.8‰ to +43.6‰, -0.09‰ to 0.09‰ and -0.50‰ to 0.56‰, respectively. Acid volatile sulphur (AVS) has $\delta^{34}S$ values from +15.3‰ to +34.8‰, $\Delta^{33}S$ values from -0.07‰ to +0.03‰ and $\Delta^{36}S$ values from -0.37‰ to +0.68‰. The CRS $\delta^{34}S$ values in the OnZap section are variable, with a slight trend towards heavier values in the upper part. Four distinct excursions exhibiting highly positive $\delta^{34}S$ values (> +30‰) occur at 17.4 m, 27.8 m, 62.4 m and 80 m depths. Throughout the section the $\delta^{34}S$ and $\Delta^{33}S$ values show an anti-correlation: where the former increases the latter shifts towards more negative values and *vice versa*. Both $\Delta^{36}S$ and $\Delta^{33}S$ display small variations and correlate negatively, defining $\Delta^{36}S/\Delta^{33}S$ arrays with a change in the slope from Unit A to Unit C (Fig. 9). In Unit A the $\Delta^{36}S/\Delta^{33}S$ array has the slope of -8 whereas the difference between Units B and C is statistically insignificant and the $\Delta^{36}S/\Delta^{33}S$ array has a slope of -4. Although the $\Delta^{36}S$-$\Delta^{33}S$ relationships show significant scatter, Unit A has a R^2 value of 0.75, whereas Units B and C show a weaker correlation, with an R^2 value of 0.46.

5. Discussion

5.1 Influence of hydrothermal alteration on geochemical signals

The presence of lava flows and gabbroic sills with peperitic contacts demonstrate that the Zaonega Formation was deposited in a magmatically active setting (Črne et al., 2013a,b; Melezhik et al., 2015). This igneous activity triggered hydrothermal circulation, generating hydrocarbons and other diagenetic fluids that permeated the sub-seafloor, altering primary mineral assemblages and catalysing secondary mineral precipitation (Melezhik et al., 1999; Qu et al., 2012; Črne et al., 2014). Thus, it is important to differentiate between depositional and/or early diagenetic geochemical signals from those that formed later. For example, detailed petrographic observations from the FAR-DEEP 12AB core revealed that hydrothermally catalysed dedolomitisation reactions produced paragenetic mineral assemblages including calcite, phlogopite and talc (Črne et al., 2014). This type of alteration is ubiquitous in Unit A of the OnZap section, with enrichments of quartz and K-feldspar, as well elevated abundances of secondary calcite and talc at lithological contacts. The FAR-DEEP 13A core, drilled ca. 300 m from the OnZap cores, contains a magmatic body at an equivalent stratigraphic level to Unit A of the OnZap section, which had the potential to sustain localised hydrothermal circulation (Črne et al., 2013a).

In contrast to Unit A, the upper part of Unit B and all of Unit C show less pronounced post-depositional alteration, and thus are more likely to preserve the most pristine mineralogical and geochemical signatures within the OnZap section. We hypothesise that the massive dolostone body at the base of Unit B (53–44 m depth) acted as a stratigraphic seal, hindering the ascent of hydrothermal fluids; an inference supported by a decrease in veining intensity, decreasing quartz, calcite and K-feldspar abundances, and an increase in iron content of the Fe/Mg-micas through Unit B and up into Unit C.

5.2 Distribution of iron in mineral phases

The conventional sequential iron extraction technique developed by Poulton and Canfield (2005), commonly referred to as "Fe speciation", is widely used to constrain depositional redox conditions based on the quantity and distribution of highly reactive iron (e.g., Poulton and Canfield, 2011). Because of the ubiquity of Fe-rich carbonate phases (dolomite to ankerite solid solution and siderite) in our samples and their known recalcitrant nature (Raiswell et al., 1994, 2012; Poulton and Raiswell, 2002; Poulton and Canfield, 2011; Clarkson et al., 2014; Slotznick et al., 2018), we used a combination of XRD and SEM-EDS analyses rather than the conventional wet-chemical extraction scheme to assess Fe partitioning in the main Fe-bearing carbonate (Fe_{Carb} = iron-rich dolomite to ankerite solid-solution phase and siderite), sulphide- (Fe_{PY} = pyrite) and silicate-phase minerals (Fe_{SIL}). This procedure is preferable in that it exploits the intrinsic physical properties of the minerals of interest and is thus not hindered by incomplete dissolution. Previous work has demonstrated that pyrrhotite in the FAR-DEEP 13A core is a product of pyrite alteration (Asael et al., 2013), hence we consider pyrrhotite as part of the Fe_{PY} pool. Iron-oxides and iron-oxyhydroxides were below the XRD quantification limit (<0.3 wt.%) in all the examined samples. We defined the silicate iron (Fe_{SIL}) pool as the sum of Fe in phyllosilicates (K-mica, Fe/Mg-mica and chlorite), the only Fe-carrying silicate phases identified in our samples.

Owing to the variable Fe contents of the varied mineral phases and types (e.g. micas and carbonates), multiple measurements by SEM-EDS were made from several representative samples from Units A, B and C. These data were then used to calculate the average iron content of the individual phases. The average iron content of muscovite-type K-mica and chlorite was found to be 3.2 and 1.6 wt.% Fe, respectively. Multiple SEM-EDS analyses demonstrated that these values were constant throughout all examined samples, whereas the iron content of Fe/Mg-mica phases was found to be variable, with low iron contents (1.4 wt.%) typifying Units A and B and high iron (20.8 wt.%) contents dominating in Unit C. Iron-rich carbonate phases

in the dolomite to ankerite solid-solution series contained up to 10 wt.% iron and were confined to the upper part of the OnZap section. Siderite, with a stoichiometric Fe abundance, is present in few samples near the top of the section. Total XRD-derived iron ($Fe_{T\text{-}XRD}$) abundances were calculated as the sum of Fe_{Carb}, Fe_{PY} and Fe_{SIL}. Generally, the calculated $Fe_{T\text{-}XRD}$ and total Fe ($Fe_{T\text{-}OES}$) determined by ICP-OES displayed a good fit ($R^2 = 0.92$); however, there are a few samples where $Fe_{T\text{-}XRD}$ diverged by more than 20% from the $Fe_{T\text{-}OES}$. This discrepancy is likely due to the higher quantification limit (~0.3–0.5 wt.%) of XRD compared to ICP-OES. Regardless, these typically iron-impoverished samples were excluded from iron distribution assessments (Supplementary Fig. 1), as recommended by previous studies (Clarkson et al., 2014). Although the XRD approach to Fe speciation is yet to be empirically calibrated, when both XRD and conventional Fe speciation approaches have been tested elsewhere there is good agreement between the two techniques (Raiswell et al., 2011), which, in the absence of full calibration (e.g., Poulton and Canfield, 2005; Clarkson et al., 2014), provide confidence in our approach.

5.3 Redox constraints on deposition in the Onega Basin

The XRD-defined Fe distribution data are illustrated in Figure 6 along with our $\delta^{13}C_{org}$ and $\delta^{34}S$ data. The raw data are given in Supplementary Table 3. Herein, the biogeochemically reactive iron pool (Raiswell et al., 1994; Poulton and Raiswell, 2002; Poulton and Canfield, 2011; Clarkson et al., 2014) is defined as $(Fe_{PY}+Fe_{Carb})/Fe_{T\text{-}XRD}$, whereas the proportion of pyrite in the reactive iron pool is defined as $Fe_{PY}/(Fe_{PY}+Fe_{Carb})$. The ratios of $(Fe_{PY}+Fe_{Carb})/Fe_{T\text{-}XRD}$ greater than 0.5 and $Fe_{PY}/(Fe_{PY}+Fe_{Carb})$ of approximately unity in OnZap Units A and B, as well as strong linear correlation between TS and $Fe_{T\text{-}OES}$ (Fig. 7), show that pyrite is the main iron-bearing phase in those strata. In Unit C, sulphur and iron concentrations show no correlation (Fig. 7) and, $(Fe_{PY}+Fe_{Carb})/Fe_{T\text{-}XRD}$ and $Fe_{PY}/(Fe_{PY}+Fe_{Carb})$ ratios are lower, albeit variable (Fig. 6). Again, strengthening the applicability of our XRD approach, the XRD-derived data are in good agreement with conventionally Fe speciation data from correlative parts of the upper Zaonega Formation (Scott et al., 2014).

If these ratios were to reflect Fe distribution patterns in the original sediment, anoxic-euxinic depositional environment would characterise Units A and B and variable redox conditions including oxic episodes would characterize Unit C. It has been shown that physical disturbance and non-steady state diagenesis of fine-grained sediments can produce highly reactive iron enrichments, even beneath an oxygenated water-mass (Aller et al., 2010). Given the complex depositional setting, featuring syn-depositional magmatism, turbidites and pervasively fluid-

influenced intervals (Unit A and lower Unit B), these data must be first treated with caution, establishing the influence of post-depositional iron mobilisation before reaching any conclusion concerning depositional redox.

Evidence for late-stage iron mobilisation is provided by the chemistry of the OnZap carbonate phases. Iron concentrations in dolomite can reach 10%, whereas secondary calcite that formed via dedolomitisation is essentially devoid of iron because of limited iron substitution and the instability of $CaFe(CO_3)_2$ solid solution series at temperatures below 450 °C (Davidson, 1994). There is, however, abundant evidence for sedimentary/early diagenetic pyrite. Petrographic observations reveal that organic-rich lamina throughout Unit A and the mudstones from Units B and C contain abundant disseminated fine-grained pyrite crystals (>10 µm) and ellipsoidal pyrite clusters (30–100 µm). Differential compaction of the organic-rich laminae around the pyrite clusters/crystals (Fig. 3a, b), and the lack of cross-cutting sedimentary fabrics, or association with quartz veins, attests to their formation early within the sediment prior to compaction and silica alteration. Carbonate beds on the other hand contain large, inclusion-laden, euhedral and anhedral pyrite crystals that clearly formed much later (Fig. 3d). Consequently, the iron distribution patterns, particularly in Unit A and the lower part of Unit B, were established within the diagenetic and metamorphic environments and cannot be used for reliably inferring water column redox conditions.

Relative to Unit A and the lower part of Unit B, Unit C and the upper part of Unit B display less evidence for post-depositional alteration. Significant part of iron in Unit C is housed in Fe-rich carbonate minerals and the increase in $Fe_{T\text{-}OES}$ coincides with the transition from a Fe-poor to a Fe-rich mica phase, reflecting less hydrothermal alteration relative to the underlying strata. Accordingly, the lower and more variable $(Fe_{PY}+Fe_{Carb})/Fe_{T\text{-}XRD}$ and $Fe_{PY}/(Fe_{PY}+Fe_{Carb})$ ratios, (Fig. 6), are a more reliable potential archive of depositional redox conditions, suggesting that the upper Zaonega Formation was deposited in a highly dynamic setting.

Scott et al. (2014) used Fe-speciation data to conclude that the upper part of the Zaonega Formation records a transition from oxic or ferruginous depositional conditions to euxinic conditions. That conclusion was based on the assumption that a complete composite stratigraphic succession of the upper Zaonega Formation was recovered by two cores: core C-5190, ~25 km south of the OnZap cores (see Fig. 1), was inferred to capture the older strata and core C-175, ~40 km south of the OnZap cores, the younger strata. Fe speciation data by those workers indicate oxic or ferruginous conditions for core C-5190 and euxinic conditions for core

C-175. However, the inference that the cores represent a composite stratigraphy is questionable. Many workers have documented a 150–200 m thick horizon containing strongly ^{13}C-depleted organic matter ($\delta^{13}C_{org}$ < -30‰) across the Onega Basin (Kump et al., 2011; Qu et al., 2012; Strauss et al, 2013; Lepland et al., 2014; Melezhik et al., 2015; Krupenik et al., 2011). In fact, Russian workers have considered it to be a basin-wide correlative marker (e.g., Filippov and Yesipko, 2016). Both cores (C-5190 and C-175) contain ^{13}C-depleted organic matter ($\delta^{13}C_{org}$ < -30‰), implying that they broadly overlap and are correlative with OnZap Units A and B. Adopting these chemostratigraphic constraints, the available Fe-speciation data are more consistent with spatially variable redox conditions across the Onega Basin, rather than a secular change in redox conditions (c.f., Scott et al., 2014). Until the relationship between cores C-5190 and C-175 is better known, especially within the wider stratigraphic context of the Zaonega Formation, their utility for global correlations and environmental interpretations remains limited.

In summary, post-depositional alteration most likely modified the iron inventory of Unit A and lower part of Unit B of the OnZap section. Unit C, by contrast, is the least altered and preserves a more primary mineral assemblage. Combining petrographic observations, with up-section trends of decreasing TOC, TS and increasing $Fe_{T\text{-}OES}$ and Fe-rich dolomite-to-ankerite solid-solution phase contents, as well as the appearance of siderite in Unit C, are consistent with a change toward more variable redox conditions. Integrating our observations with the findings of others indicates that the upper Zaonega Formation inherited its Fe inventory under spatially and temporally variable depositional and diagenetic conditions, as would be expected in a magmatically active and seep-influenced setting. In total, our data indicate that euxinia was not as pervasive in the upper part of the Zaonega Formation as suggested previously (Scott et al., 2014) and, in fact, conditions may have been episodically oxic.

5.4 Biogeochemical sulphur cycling

5.4.1 Hydrothermal influence on the Zaonega Formation sulphides

Sulphide minerals in marine settings with active hydrothermal circulation can be produced by several mechanisms and may have sulphur-isotope values that reflect contemporaneous but unrelated processes (Aoyama et al., 2014; Eickmann et al., 2014). For example, modern seawater sulphate is typically marked by positive $\delta^{34}S$ (+21.5‰) and $\Delta^{33}S$ (+0.04‰) values (Ono et al., 2012; Johnston et al., 2014; Tostevin et al., 2014; Masterson et al., 2016), whereas deep sourced hydrothermal fluids have values closer to primordial sulphur ($\delta^{33}S = \delta^{34}S = \delta^{36}S$

= 0‰; Ono et al., 2006, 2007, 2012). Furthermore, mass-dependent fractionations of up to 4‰ in $\delta^{34}S$ and 0.07‰ in $\Delta^{33}S$ can be imparted under certain oxygen fugacities and oxidation reactions in magmatic and hydrothermal systems (Fiorentini et al., 2012; Ono et al., 2007; Penniston-Dorland et al., 2012; Ripley et al., 2017). Thus, in a setting such as that in which the Zaonega Formation was deposited, care must be taken when ascribing a pyrite sulphur isotope value to a seawater sulphate source.

Several features of our sulphur isotope data, particularly the negative excursions, warrant exploration. A prominent negative $\delta^{34}S$ excursion to ~ 0‰ within silicified mudstones at 77–70 m depth is accompanied by distinctly positive $\Delta^{33}S$ values of ~+0.05‰ (Fig. 6). Three additional negative $\delta^{34}S$ excursions to values below +5‰ punctuate the OnZap section. These, excursions occur at lithological boundaries between carbonate and mudstone beds at 86, 46 and 32 m depth. Of these, those at 85 m and 32 m also exhibit positive >+0.05 $\Delta^{33}S$ values. Pyrites associated with these shifts have different origins and may reflect different processes in space and time. Euhedral crystals associated with compacted sedimentary laminae, along with minute octahedral pyrite crystals, were precipitated early in unconsolidated sediments. By contrast, large inclusion-rich euhedral crystals that occur with minor sphalerite and pyrrhotite crystals, particularly in Units A and B, suggest later post-depositional pyrite formation as noted also by Asael et al. (2013). There are a variety of explanations for the observed negative S-isotope excursions. For example, the addition of hydrothermally derived sulphur could account for the observed $\delta^{34}S$ shift toward 0‰ but would not explain a positive shift in $\Delta^{33}S$ seen in the silicified interval at 77–70 m. Alternatively, there may have been short-lived, more open-system conditions that would have allowed the expression of larger microbially-induced S-isotope fractionation. Otherwise, iron limitation could also have conceivably lowered $\delta^{34}S$ values by limited sulphide sequestration to the initially produced, and presumably most ^{34}S-depleted, sulphide.

We note that post-depositional isotope effects associated with pyrite remobilisation and AVS formation depend on the temperature and oxidation state of the percolating fluid and hence is difficult to constrain precisely (Wagner and Boyce, 2006). With few exceptions, the isotopic composition of AVS is only separated from the CRS by a few per mil, thus the fluids interacting with the Zaonega rocks were sufficiently reducing and were unlikely to have promoted large-magnitude sulphur isotope fractionations during pyrite recrystallisation (Fig. 6). On the other hand, it is possible that recrystallisation homogenised the sulphur isotope composition of the

early-formed small pyrite crystals and clusters masking the extreme variability of individual crystals that are characteristic for modern seep environments (Lin et al., 2016).

Thermochemical sulphate reduction (TSR) could also serve as a mechanism for precipitating secondary pyrites (Watanabe et al., 2009; Oduro et al., 2011). The Zaonega Formation is underlain by the evaporite-bearing Tulomozero Formation (Reuschel et al., 2012; Blättler et al., 2018). It is possible, therefore, that hydrothermal fluids could have leached sulphur from the underlying evaporites, which could induce precipitation of late-stage pyrite upon reduction in contact with the organic-rich strata of the Zaonega Formation. However, the Tulomozero Ca-sulphate evaporites have $\delta^{34}S$ values ranging from +6 to +10‰ and $\Delta^{33}S$ values of ~0‰ (Reuschel et al., 2012; Blättler et al., 2018) which are not compatible with the combination of S-isotope values encasing the negative excursions. Although progressive TSR could lead to ^{34}S enrichments of sulphur-bearing fluids and Rayleigh distillation effects (Watanabe et al., 2009). Oduro et al. (2011) demonstrated that TSR is associated with a mass-independent magnetic isotope effect which influence odd-numbered isotope (^{33}S), generating $\Delta^{36}S/\Delta^{33}S$ slopes that deviate from thermodynamic predictions ($\Delta^{36}S/\Delta^{33}S$ slope of ~7; Ono et al., 2006). Thus, TSR is not consistent with the $\Delta^{36}S/\Delta^{33}S$ slope of ~-8 observed in Unit A which is more typical for MSR (Johnston et al., 2005a, 2007).

Although the $\Delta^{36}S$-$\Delta^{33}S$ relationship is more scattered in Units B and C, these intervals are relatively low in TOC, AVS is scarce and evidence for post-depositional alteration is infrequent, rendering TSR unlikely. Furthermore, progressive TSR of ascending fluids would cause vertical and lateral $\delta^{34}S$ and $\Delta^{33}S$ gradients, which are not observed in the OnZap pyrite record. We do note that, while a magmatic sulphur source for explaining the four negative $\delta^{34}S$ and positive $\Delta^{33}S$ excursions is unlikely, ambient seawater percolating in the sediments could have provided a sulphur source, localising TSR for secondary pyrite formation. With the available data, we cannot unequivocally preclude secondary processes, however, their effect appears to have been limited. The four negative $\delta^{34}S$ shifts can most likely be explained by syndepositional and early diagenetic processes such as changes in the openness of the pore water with respect to the overlying water column or Fe availability. Further investigation by secondary ion mass-spectrometry (SIMS) could test these competing hypotheses, and provide insight beyond the bulk approach leveraged herein.

5.4.2 Carbon and sulphur isotope records of microbial processes

Given the preceding discussion, we interpret the sedimentary pyrites of the upper Zaonega Formation as the product of sediment-hosted MSR, rather than direct precipitates from an euxinic water column (e.g. Scott et al., 2014). Previous work (Qu et al., 2012; Lepland et al., 2014) has shown that the Zaonega sediments were deposited in a magmatically active setting with syndepositional hydrocarbon migration and venting. Such a nutrient replete environment likely sustained microbial activity in the water column, at the seafloor and in the shallow sub-surface, in turn creating sharp chemoclines and a complex seafloor ecosystem of sulphur oxidisers and methanotrophic archaea. Evidence for migrating hydrocarbons is preserved as numerous pyrobitumen veins and nodules that occur variably throughout the Zaonega succession, including the OnZap section (e.g. nodules at 54 m depth). Comparisons of $\delta^{13}C_{org}$ in the host rock and cross-cutting pyrobitumen veins have demonstrated only minor differences (< 0.5‰) in the FAR-DEEP 12AB core indicating a hydrocarbon source in adjacent organic-rich sediments (e.g. Qu et al., 2012, 2018). Far-travelled hydrocarbon migration can be precluded because there is no other known source of highly ^{13}C-depleted material in the Onega Basin. Moreover, thermal cracking of organic matter will exclusively shift the preserved $\delta^{13}C_{org}$ to more positive values (Hayes, 1983; Lewan, 1983; Clayton, 1991; Schidlowski, 2001), the opposite of what is seen. Thus, it appears likely that the highly ^{13}C-depleted organic matter in Units A and Unit B contains a significant methanotrophic component.

As anaerobic methanotrophy coupled to sulphate reduction (anaerobic oxidation of methane; AOM) proceeded, conditions in the diagenetic environment would have become increasingly sulphidic, driving the redox interface closer to the sediment-water interface. A combination of elevated methane and high biomass burial flux will have intensified pore-water sulphate reduction rates, possibly exceeding diffusive replenishment from above (Goldhaber and Kaplan, 1975; Jørgensen, 1979, 2004). Such a scenario would have resulted in the near quantitative uptake of sulphate, muting the fractionation expressed between the initial sulphate and product sulphide. Complete reduction of the available pore water sulphate pool would produce sulphides with $\delta^{34}S$ values that approximate or even exceed those of the initial seawater sulphate (Pasquier et al., 2017). During the Paleoproterozoic, MSR is thought to have been the main sulphur utilising metabolism (Canfield and Teske, 1996; Johnston et al., 2005b, 2006, 2011). Pure culture studies of sulphate reducers have shown that, as MSR proceeds under sulphate limiting conditions, the sulphate $\delta^{34}S$ values increase whereas the $\Delta^{33}S$ values decrease relative to the starting sulphate (Johnston et al., 2005a). When plotted on a $\delta^{34}S$ vs $\Delta^{33}S$ three-

isotope plot, our sulphur isotope data mostly populate quadrant II (Fig. 8), which is indicative of MSR (Johnston et al., 2005a, b, 2007; Sim et al., 2011). This, however, does not necessarily exclude the presence of sulphur oxidisers, since sulphide oxidation results in much smaller sulphur isotope fractionations than MSR and it is possible that the signal for sulphur oxidation was not preserved and/or is masked within the sediments (Balci et al., 2007; Zerkle et al., 2009, 2016).

We propose that the inverse covariation between pyrite $\delta^{34}S$ and $\Delta^{33}S$ and the values that deviate from that trend (i.e. positive $\delta^{34}S$ and $\Delta^{33}S$) observed in our data reflect an organic-rich seafloor or shallow subsurface diagenetic environment where sulphate was readily available, but under high demand, and rapidly consumed. Most of our $\delta^{34}S$ and $\Delta^{33}S$ values vary from +15‰ to +25‰ and -0.05‰ to -0.02‰, respectively, with some slight variation ($\delta^{34}S$ 20.2 ± 3.2‰ and $\Delta^{33}S$ -0.03 ± 0.01‰, 1σ). Such isotopic stability in sedimentary sulphides requires an almost constant sulphate flux with a uniform isotopic composition. Thus, the sulphate pool had to be large enough to maintain high rates of sulphate reduction. Additionally, there is a clear statistically significant (p <0.05) negative correlation between $\Delta^{33}S$ and $\Delta^{36}S$ (Fig. 9): in Unit A, $\Delta^{36}S = -7.66*\Delta^{33}S - 0.08$, $R^2=0.75$; in Units B and C $\Delta^{36}S = -4.10*\Delta^{33}S - 0.15$, $R^2=0.46$. These small magnitude $\Delta^{33}S$ and $\Delta^{36}S$ values, and the observed co-variation between $\Delta^{33}S$ and $\Delta^{36}S$, approximate the theoretically predicted $\Delta^{36}S/\Delta^{33}S$ ratio for mass-dependent low-temperature processes (~-7; Ono et al., 2006; Farquhar et al., 2007; Johnston et al., 2007). Moreover, although the $\Delta^{36}S/\Delta^{33}S$ array recorded in Unit A deviates slightly from the equilibrium prediction, it is in the range of values measured for sulphate reduction in natural settings (between -11 and -5; Johnston et al., 2007, 2008) and is thus consistent with MSR being the dominant active sulphur-utilising metabolism in the lower part of the OnZap section. Given that closed-system isotope effects may influence the relationship between $\Delta^{33}S$ and $\Delta^{36}S$, whilst generating large variability in $\delta^{34}S$ (Ono et al., 2006; Johnston et al., 2007), the up-section increase in the $\Delta^{36}S/\Delta^{33}S$ ratios (~ -4 in Units B and C) could relate to such effects.

5.4.3 Conditions during deposition of relatively organic-poor Unit C

Unit C, the uppermost interval of the OnZap cores, represents a newly recovered and unstudied part of the Zaonega Formation. This ca. 25-m-thick interval is marked by parallel-laminated to ripple cross-laminated grey mudstones and dolostone beds that are less organic-rich than those in underlying units. Unit C also lacks evidence for hydrocarbon generation or migration. There is a slight trend towards more positive $\delta^{34}S$ values accompanied by a positive shift in $\delta^{13}C_{org}$ from -38‰ to -25‰ and a decrease in TOC and TS. We interpret this trend as indicating a

decreasing contribution from methanotrophic biomass in favour of more typical CO_2-fixing autotrophic biomass contributing to the C-isotopic signatures of Unit C. As the hydrocarbon flux decreased, sulphate reducing microbes capable of utilising both methane (AOM) and organic carbon as electron donors (Joye et al., 2004), could have switched to solely organic carbon. Despite changes in the microbial community, the TOC content in Unit C (≤ 3 wt.%) is sufficiently high to have sustained sulphate reduction. A waning hydrocarbon flux would have shifted the redox interface deeper into the sediments where the availability of labile organic matter, iron concentrations and connectivity of pore waters to the overlying water column could have influenced sulphate reduction rates and the extent of S isotope fractionation between sulphate and sulphide (Zaback et al., 1993; Sim et al., 2011; Fike et al., 2015). The most variable $\delta^{34}S$, $\Delta^{33}S$, $\Delta^{36}S/\Delta^{33}S$ ratios and the highest ^{34}S-enrichments (outside Unit A) are found in Unit C. These may represent Rayleigh-type effects either in the sediments or indicate episodes of at least partial basinal isolation from the open ocean.

Most pyrites from the OnZap section exceed the lower estimate for SWS isotope composition of $\delta^{34}S$ ~+10‰ and $\Delta^{33}S$ ~0‰ derived from the underlying Ca-sulphate evaporites of the Tulomozero Formation (Reuschel et al., 2012; Blättler et al., 2018). In ancient pyrite records, sulphides with $\delta^{34}S$ values that exceed SWS are typically interpreted to reflect enhanced pyrite burial or changes in the marine sulphate reservoir (Goldhaber and Kaplan, 1975; Johnston et al., 2006, 2008; Gomes and Hurtgen, 2013; Fike et al., 2015). However, it has been highlighted that the decoupling of pore water and seawater sulphate reservoirs via sedimentary and diagenetic mechanisms can also produce highly ^{34}S-enriched pyrites approaching and, rarely, even exceeding the seawater $\delta^{34}S$ value (Aller et al., 2010; Fike et al., 2015; Pasquier et al., 2017). Within the tectonically active Onega Basin it is likely that a combination of changes in microbial metabolic activity and sulphate mobility into the sediment pile resulted in the near quantitative reduction of sulphate into sulphide.

The Onega Basin has experienced major variations in basinal configuration throughout its history. Lower part of the underlying Tulomozero Formation with >800 m thick evaporate succession revealed in Onega Parametric Hole captures one of such episodes in Onega Basin history where a restricted marine embayment with sabkha/coastal plain was developed (Krupeinik et al., 2011; Blättler et al., 2018). The exact palaeogeography of the Onega Basin during Zaonega time is not known but it is possible that episodic volcanic activity could have created barriers that impeded water mass exchange between the Onega Basin and the open ocean. In such a setting, it is conceivable that constriction of the hydrographic connection

between the Onega Basin and the wider global ocean would result in a smaller sulphate reservoir that would be more susceptible to sulphate drawdown and closed-system effects (e.g. Gomes, 2013; Fike et al., 2015). The occurrence of abundant Fe-rich dolomite to ankerite solid-solution phase and siderite in Unit C might also imply a limited sulphate pool (Moore et al., 1992). Such conditions would result in low pore water sulphide availability that would favour Fe^{2+} incorporation into carbonate phase(s). Speculatively, the four $\delta^{34}S$ positive excursions in the OnZap section, rising from ~+20‰ to > +30‰, followed by a return to ~+20‰, could represent such repeated expansions and contractions in the sulphate reservoir in pore waters and/or the overlying seawater.

Thus, changes in microbial metabolic rates and communities, pore water connectivity and basinal sulphate concentrations may all be imprinted into the Zaonega Formation C_{org}- and S-isotope record. Previous workers have used the latter to argue for a postulated decrease in atmospheric oxygen driving a decrease in global SWS concentrations (e.g. Scott et al., 2014). Our new and more comprehensive geochemical dataset offers an alternative explanation, one not dependent on equivocal assumptions about long-distance correlations and assumed temporal equivalence. We argue that the relatively consistent pyrite $\delta^{34}S$ (~20‰) and $\Delta^{33}S$ (-0.03‰) values are best explained by a stable flux of sulphate into the sediments and rapid MSR. These conditions would track fluctuations in basinal sulphate isotope composition and, thus, the Zaonega sulphur isotope record is most parsimoniously explained as reflecting local (basin-scale) conditions under closed-system behaviour rather than a global-scale phenomenon.

7. Conclusions

Detailed lithological, mineralogical and geochemical observations of the recently drilled 102-m thick OnZap core encompassing the upper Zaonega Formation show that the organic-rich mudstones and carbonate beds in the lower part of the section were deposited coevally with mafic volcanism. This created a dynamic setting of high heat flux, hydrocarbon migration and abundant nutrients that stimulated microbial activity within the sediments. In the lower Zaonega Formation elevated TOC, TS, abundant sulphide minerals and ^{13}C-depleted organic matter ($\delta^{13}C_{org}$ < -30‰) are all consistent with basin-wide methanotrophy and a high sulphate demand. High rates of pore-water MSR fuelled quantitative conversion of sulphate to sulphide causing pyrite to become increasingly enriched in ^{34}S and approach the $\delta^{34}S$ of the precursor sulphate. In contrast, the finely laminated grey mudstone and marly dolostone beds in the uppermost part of the Zaonega Formation record more variable redox conditions in a partially isolated/closed-

system basin setting. The decrease in TOC and TS abundances and less negative $\delta^{13}C_{org}$ at the top of the section likely reflect changes in the microbial community, as methanotrophs were superseded by CO_2-fixing autotrophs in response to a waning hydrocarbon flux. The excursion towards $\delta^{34}S$ values that exceed +30‰ are best interpreted as recording changing basinal conditions rather than changes in global seawater sulphate concentrations. Our findings highlight the culmination of microbial and basin-specific processes (magmatic activity, hydrocarbon seepage, sedimentary processes and basinal restriction), suggesting that these local- to regional-scale processes dominated the sulphur isotope record of the Paleoproterozoic Zaonega Formation.

Acknowledgements

We are grateful to Harry Oduro for initial advice on pyrite extractions and Boswell A. Wing for valuable discussions and laboratory use at McGill University. David Fike and an anonymous reviewer are thanked for conversations and constructive comments that have greatly improved the manuscript. We acknowledge Andrey Bekker, Timothy W. Lyons and Clint Scott who helped to improve an earlier version of the manuscript. The research is part of the Centre for Arctic Gas Hydrate, Environment and Climate and was supported by the Research Council of Norway through its Centres of Excellence funding scheme grant No. 223259. A. L. Z. acknowledges support from a Natural Environment Council Standard Grant NE/J023485/2. G. I. acknowledges the Simons Collaboration on the Origins of Life for support during the final drafting stages of this manuscript. K. K, A. L, T. K and K. M. were supported by the Estonian Science Agency grant PUT696 and Estonian Center of Analytical Chemistry. We appreciate the work by Rona McGill on organic carbon isotope analyses by the NERC Life Sciences Mass Spectrometry Facility at the Scottish Universities Environmental Research Centre.

References

Aller, R.C., Madrid, V., Chistoserdov, A., Aller, J.Y., and Heilbrun, C. (2010) Unsteady diagenetic processes and sulphur biogeochemistry in tropical deltaic muds: Implications for oceanic isotope cycles and the sedimentary record. *Geochimica et Cosmochimica Acta* 74, 4671–4692.

Aoyama S., Nishizawa M., Takai K. and Ueno Y. (2014) Microbial sulfate reduction within the Iheya North subseafloor hydrothermal system constrained by quadruple sulfur isotopes. *Earth and Planetary Science Letters* 398, 113–126.

Asael D., Tissot F.L.H., Reinhard C.T., Rouxel O., Dauphas N., Lyons T.W., Ponzevera E., Liorzou, C. and Cheron, S. (2013) Coupled molybdenum, iron and uranium stable isotopes as oceanic paleoredox proxies during the Paleoproterozoic Shunga Event. *Chemical Geology* 362, 193–210.

Balci N., Shanks W. C., Mayer B. and Mandernack K. W. (2007) Oxygen and sulfur isotope systematics of sulfate produced by bacterial and abiotic oxidation of pyrite. *Geochimica et Cosmochimica Acta* 71, 3796–3811.

Bekker A., Holland H. D., Wang P. L., Rumble D., Stein H. J., Hannah J. L., Coetzee L. L. and Beukes N. J. (2004) Dating the rise of atmospheric oxygen. *Nature* 427, 117–120.

Bekker A., Karhu J. A., Eriksson K. A., Kaufman A. J. (2003) Chemostratigraphy of Paleoproterozoic carbonate successions of the Wyoming Craton: tectonic forcing of biogeochemical change? *Precambrian Research* 120, 279–325.

Bekker A., Karhu J. A., Kaufman A. J., (2006) Carbon isotope record for the onset of the Lomagundi carbon isotope excursion in the Great Lakes area, North America. *Precambrian Research* 148, 145–180.

Blättler, C.L., Claire, M.W., Prave, A.R., Kirsimäe, K., Higgins, J.A., Medvedev, P.V., Romashkin, A.E., Rychanchik, D.V., Zerkle, A.L., Paiste, K., Kreitsmann, T., Millar, I.L., Hayles, J.A., Bao, H., et al., 2018, Two-billion-year-old evaporites capture Earth's great oxidation: *Science*, p. eaar2687.

Bradley A. S., Leavitt W. D., Schmidt M., Knoll A. H., Girguis P. R. and Johnston D. T. (2016) Patterns of sulfur isotope fractionation during microbial sulfate reduction. *Geobiology* 14, 91–101.

Brüchert V. (2004) Physiological and ecological aspects of sulfur isotope fractionation during bacterial sulfate reduction, in: Special Paper 379: Sulfur Biogeochemistry - Past and Present. *Geological Society of America*, 1–16.

Canfield D. E. and Teske A. (1996) Late Proterozoic rise in atmospheric oxygen concentration inferred from phylogenetic and sulphur-isotope studies. *Nature* 382, 127–132.

Canfield D. E., Farquhar J. and Zerkle A. L. (2010) High isotope fractionations during sulfate reduction in a low-sulfate euxinic ocean analog. *Geology* 38, 415–418.

Canfield D. E., Raiswell R., Westrich J. T., Reaves C. M. and Berner R. A. (1986) The use of chromium reduction in the analysis of reduced inorganic sulfur in sediments and shales. *Chemical Geology* 54, 149–155.

Canfield D. E., Thamdrup B. (1994) The Production of S-34-Depleted Sulfide during Bacterial Disproportionation of Elemental Sulfur. *Science* 266, 1973–1975.

Clarkson M. O., Poulton S. W., Guilbaud R. and Wood R. A. (2014) Assessing the utility of Fe/Al and Fe-speciation to record water column redox conditions in carbonate-rich sediments. *Chemical Geology* 382, 111–122.

Črne A. E., Melezhik V. A., Lepland A., Fallick A. E., Prave A. R. and Brasier A. T. (2014) Petrography and geochemistry of carbonate rocks of the Paleoproterozoic Zaonega Formation, Russia: Documentation of C-13-depleted non-primary calcite. *Precambrian Research* 240, 79–93.

Črne A. E., Melezhik V. A., Prave A. R., Lepland A., Romashkin A. E., Rychanchik D. V., Hanski E. J. and Luo Z. (2013a) Zaonega Formation: FAR-DEEP Hole 13A, in: Melezhik V. A., Prave A. R., Fallick A. E., Hanski E. J., Lepland A., Kump L. R., Strauss H. (Eds.), *Reading the Archive of Earth's Oxygenation: Volume 2: The Core Archive of the Fennoscandian Arctic Russia - Drilling Early Earth Project*. Springer, 1008–1046.

Črne A.E., Melezhik V.A., Prave A.R., Lepland A., Romashkin A.E., Rychanchik D.V., Hanski E.J. and Luo Z. (2013b) Zaonega Formation: FAR-DEEP Holes 12A and 12B, and Neighbouring quarries, in: Melezhik V. A., Prave A. R., Fallick A. E., Hanski E. J., Lepland A., Kump L. R., Strauss H. (Eds.), *Reading the Archive of Earth's Oxygenation: Volume 2: The Core Archive of the Fennoscandian Arctic Russia - Drilling Early Earth Project*. Springer, 946–1007.

Davidson P.M. (1994) Ternary iron, magnesium, calcium carbonates; a thermodynamic model for dolomite as an ordered derivative of calcite-structure solutions. *American Mineralogist* 79, 332–339.

Detmers J., Brüchert V., Habicht K.S., and Kuever J. (2001) Diversity of sulfur isotope fractionations by sulfate-reducing prokaryotes. *Applied and Environmental Microbiology* 67, 888–894.

Eickmann B., Thorseth I. H., Peters M., Strauss H., Brocker M. and Pedersen R. B. (2014) Barite in hydrothermal environments as a recorder of subseafloor processes: a multiple-isotope study from the Loki's Castle vent field. *Geobiology* 12, 308–321.

Farquhar J., Johnston D. T., Wing B. A., (2007) Implications of conservation of mass effects on mass-dependent isotope fractionations: Influence of network structure on sulfur isotope phase space of dissimilatory sulfate reduction. *Geochimica et Cosmochimica Acta* 71, 5862–5875.

Farquhar J., Johnston D. T., Wing B. A., Habicht K. S., Canfield D. E., Airieau S. and Thiemens M. H. (2003) Multiple sulphur isotopic interpretations of biosynthetic pathways: implications for biological signatures in the sulphur isotope record. *Geobiology* 1, 27–36.

Fike D. A., Bradley A. S. and Rose C. V. (2015) Rethinking the Ancient Sulfur Cycle. *Annual Review of Earth and Planetary Sciences* 43, 593–622.

Filippov M.M. and Yesipko O. A. (2016) Geological-geophysical marker horizons of the Paleoproterozoic Onega Structure. Karelian Science Centre, Russian Academy of Sciences, Petrozavodsk, 257 p (in Russian).

Fiorentini M.L., Bekker A., Rouxel O., Wing B.A., Maier W., and Rumble D. (2012) Multiple Sulfur and Iron Isotope Composition of Magmatic Ni-Cu-(PGE) Sulfide Mineralization from Eastern Botswana. *Economic Geology* 107, 105–116.

Galdobina, L.P., 1987, The Ludikovi superhorizon, in Sokolov, V.A. ed., Geology of Karelia. *Nauka (Science), Leningrad,* 59–67.

Goldhaber M. B. and Kaplan I. R. (1975) Controls and consequences of sulfate reduction rates in recent marine sediments. *Soil Science,* 119.

Gomes M. L., Hurtgen M. T. (2013) Sulfur isotope systematics of a euxinic, low-sulfate lake: Evaluating the importance of the reservoir effect in modern and ancient oceans. *Geology* 41, 663–666.

Gumsley A. P., Chamberlain K. R., Bleeker W., Soderlund U., Kock M. D. O., Larsson E. R., Bekker A. (2017) Timing and tempo of the Great Oxidation Event. *Proceedings of the National Academy of Sciences USA* 114, 1811–1816.

Guo Q. J., Strauss H., Kaufman A. J., Schroder S., Gutzmer J., Wing B., Baker M. A., Bekker A., Jin Q. S., Kim S. T., Farquhar J., 2009. Reconstructing Earth's surface oxidation across the Archean-Proterozoic transition. *Geology* 37, 399–402.

Habicht K. S., Gade M., Thamdrup B., Berg P. and Canfield D. E. (2002) Calibration of sulfate levels in the Archean Ocean. *Science* 298, 2372–2374.

Holland H. D. (2006) The oxygenation of the atmosphere and oceans. *Philosophical Transactions of the Royal Society B* 361, 903–915.

Johnston D. T., Farquhar J. and Canfield D. E. (2007) Sulfur isotope insights into microbial sulfate reduction: When microbes meet models. *Geochimica et Cosmochimica Acta* 71, 3929–3947.

Johnston D. T., Farquhar J., Wing B. A., Kaufman A., Canfield D. E. and Habicht K. S. (2005a) Multiple sulfur isotope fractionations in biological systems: A case study with sulfate reducers and sulfur disproportionators. *American Journal of Science* 305, 645–660.

Johnston D. T., Gill B. C., Masterson A., Beirne E., Casciotti K. L., Knapp A. N., Berelson W. (2014) Placing an upper limit on cryptic marine sulphur cycling. *Nature* 513, 530.

Johnston D. T., Poulton S. W., Fralick P. W., Wing B. A., Canfield D. E. and Farquhar J. (2006) Evolution of the oceanic sulfur cycle at the end of the Paleoproterozoic. *Geochimica et Cosmochimica Acta* 70, 5723–5739.

Johnston D. T., Wing B. A., Farquhar J., Kaufman A. J., Strauss H., Lyons T. W., Kah L. C. and Canfield D. E. (2005b) Active microbial sulfur disproportionation in the Mesoproterozoic. *Science* 310, 1477–1479.

Johnston D.T. (2011) Multiple sulfur isotopes and the evolution of Earth's surface sulfur cycle. *Earth-Science Reviews* 106, 161–183.

Johnston D.T., Farquhar J., Habicht K.S., Canfield D.E. (2008) Sulphur isotopes and the search for life: strategies for identifying sulphur metabolisms in the rock record and beyond. *Geobiology* 6, 425–435.

Jørgensen B. B. (1979) A theoretical model of the stable sulfur isotope distribution in marine sediments. *Geochimica et Cosmochimica Acta* 43, 363–374

Jørgensen B. B., Bottcher M. E., Luschen H., Neretin L. N. and Volkov I. I. (2004) Anaerobic methane oxidation and a deep H2S sink generate isotopically heavy sulfides in Black Sea sediments. *Geochimica et Cosmochimica Acta* 68, 2095–2118.

Joye S. B., Boetius A., Orcutt B. N., Montoya J. P., Schulz H. N., Erickson M. J., Lugo S. K. (2004) The anaerobic oxidation of methane and sulfate reduction in sediments from Gulf of Mexico cold seeps. *Chemical Geology* 205, 219–238.

Karhu J. A. and Holland H. D. (1996) Carbon isotopes and the rise of atmospheric oxygen. *Geology* 24, 867–870.

Krupenik V. A., Akhmedov A. M. and Sveshnikova K. Y. (2011) Isotopic composition of carbon, oxygen and sulfur in the Ludicovian and Jatulian rocks, in: Glushanin L. V., Sharov N. V., Shchiptsov V. V. (Eds.), *The Onega Paleoproterozoic Structure (Geology, Tectonics, Deep Structure, Minerogeny)*. Institute of Geology, Karelian Research Centre RAS, Petrozavodsk, 250–255 (in Russian).

Kump L. R., Junium C., Arthur M. A., Brasier A., Fallick A., Melezhik V., Lepland A., Crne A. E. and Luo G. (2011) Isotopic Evidence for Massive Oxidation of Organic Matter Following the Great Oxidation Event. *Science* 334, 1694–1696.

Lepland A., Joosu L., Kirsimae K., Prave A. R., Romashkin A. E., Crne A. E., Martin A. P., Fallick A. E., Somelar P., Upraus K., Mand K., Roberts N. M. W., van Zuilen M. A., Wirth R. and Schreiber A. (2014) Potential influence of sulphur bacteria on Palaeoproterozoic phosphogenesis. *Nature Geoscience* 7, 20–24.

Lepland A., Melezhik V. A., Papineau A. E., Romashkin A. E. and Joosu L. (2013) The Earliest Phosphorites – Radical Change in the Phosphorus Cycle during the Palaeoproterozoic, in: Melezhik V. A., Prave A. R., Fallick A. E., Kump L. R., Strauss H., Lepland A., Hanski E. (Eds.), *Reading the Archive of Earth's Oxygenation: Volume 3: Global Events and the Fennoscandian Arctic Russia - Drilling Early Earth Project*. Springer, 1275–1296.

Lin Z., Sun X., Lu Y., Xu L., Gong J., Lu H., Teichert B. M. A., Peckmann J. (2016) Stable isotope patterns of coexisting pyrite and gypsum indicating variable methane flow at a

seep site of the Shenhu area, South China Sea. *Journal of Asian Earth Sciences* 123, 213–223.

Luo G. M., Ono, S. H., Beukes, N. J., Wang, D. T., Xie, S. C., Summons, R. E. (2016) Rapid oxygenation of Earth's atmosphere 2.33 billion years ago. *Science Advances* 2.

Martin, A. P., Condon, D. J., Prave, A. R., and Lepland, A. (2013) A review of temporal constraints for the Palaeoproterozoic large, positive carbonate carbon isotope excursion (the Lomagundi–Jatuli Event). *Earth-Science Reviews* 127, 242–261.

Martin A. P., Prave A. R., Condon D. J., Lepland A., Fallick A. E., Romashkin A. E., Medvedev P. V. and Rychanchik D. V. (2015) Multiple Palaeoproterozoic carbon burial episodes and excursions. *Earth and Planetary Science Letters* 424, 226–236.

Masterson A. L., Wing B. A., Paytan A., Farquhar J. and Johnston D. T. (2016) The minor sulfur isotope composition of Cretaceous and Cenozoic seawater sulfate. *Paleoceanography* 31, 779–788.

Melezhik V. A., Fallick A. E., Filippov M. M. and Larsen O. (1999) Karelian shungite - an indication of 2.0-Ga-old metamorphosed oil-shale and generation of petroleum: geology, lithology and geochemistry. *Earth-Science Reviews* 47, 1–40.

Melezhik V. A., Fallick A. E., Filippov M. M., Deines Y. E., Črne A. E., Lepland A., Brasier A. T. and Strauss H. (2013a) Giant Palaeoproterozoic Petrified Oil Field in the Onega Basin, in: Melezhik V. A., Prave A. R., Fallick A. E., Kump L. R., Strauss H., Lepland A., Hanski E. J. (Eds.), *Reading the Archive of Earth's Oxygenation: Volume 3: Global Events and the Fennoscandian Arctic Russia - Drilling Early Earth Project*. Springer, 1202–1212.

Melezhik V. A., Filippov M. M. and Romashkin A. E. (2004) A giant Palaeoproterozoic deposit of shungite in NW Russia: genesis and practical applications. *Ore Geology Reviews* 24, 135–154.

Melezhik V. A., Medvedev P. V. and Svetov S. A. (2013b) The Onega Basin, in: Melezhik V. A., Prave A. R., Hanski E. J., Fallick A. E., Lepland A., Kump L. R., Strauss H. (Eds.), *Reading the Archive of Earth's Oxygenation: Volume 1: The Paleoproterozoic of Fennoscandia as Context for the Fennoscandian Arctic Russia - Drilling Early Earth Project*. Springer, 249–287.

Melezhik V.A., Fallick A.E., Brasier A.T., and Lepland, A. (2015) Carbonate deposition in the Palaeoproterozoic Onega basin from Fennoscandia: a spotlight on the transition from the Lomagundi-Jatuli to Shunga events. *Earth-Science Reviews* 147, 65–98.

Moore S. E., Ferrell R. E., Ahron P. (1992) Diagenetic siderite and other ferroan carbonates in a modern subsiding marsh sequence. *Journal of Sedimentary Research* 62, 357–366.

Morozov A. F., Hakhaev B. N., Petrov O. V., Gorbachev V. I., Tarkhanov G. B., Tsvetkov L. D., Erinchek Y. M., Akhmedov A. M., Krupenik V. A. and Sveshnikova K. Y. (2010) Rock-salts in Palaeoproterozoic strata of the Onega depression of Karelia (based on data from the Onega parametric drillhole). *Transection of Academy of Sciences* 435, 230–233 (in Russian).

Oduro H., Harms B., Sintim H.O., Kaufman A.J., Cody G., Farquhar J. (2011) Evidence of magnetic isotope effects during thermochemical sulfate reduction. *Proceedings of the National Academy of Sciences* 108, 17635–17638.

Oduro H., Kamyshny A., Zerkle A. L., Li Y., Farquhar J. (2013) Quadruple sulfur isotope constraints on the origin and cycling of volatile organic sulfur compounds in a stratified sulfidic lake. *Geochimica et Cosmochimica Acta* 120, 251–262.

Ohmoto H., Watanabe Y., Lasaga A. C., Naraoka H., Johnson I., Brainard, J., Chorney A. (2014) Oxygen, iron, and sulfur geochemical cycles on early Earth: Paradigms and contradictions, in: Shaw G. H., *Earth's Early Atmosphere and Surface Environment*. Geological Society of America, 55–95.

Ojakangas R. W., Marmo J. S. and Heiskanen K. I. (2001) Basin evolution of the Paleoproterozoic Karelian Supergroup of the Fennoscandian (Baltic) Shield. *Sedimentary Geology* 141, 255–285.

Ono S. H., Keller N. S., Rouxel O. and Alt J. C. (2012) Sulfur-33 constraints on the origin of secondary pyrite in altered oceanic basement. *Geochimica et Cosmochimica Acta* 87, 323–340.

Ono S., Shanks W. C., Rouxel O. J. and Rumble D. (2007) S-33 constraints on the seawater sulfate contribution in modern seafloor hydrothermal vent sulfides. *Geochimica et Cosmochimica Acta* 71, 1170–1182.

Ono S., Wing B., Johnston D., Farquhar J. and Rumble D. (2006) Mass-dependent fractionation of quadruple stable sulfur isotope system as a new tracer of sulfur biogeochemical cycles. *Geochimica et Cosmochimica Acta* 70, 2238–2252.

Ossa-Ossa F., Eickmann B., Hofmann A., Planavsky N. J., Asael D., Pambo F., and Bekker A. (2018) Two-step deoxygenation at the end of the Paleoproterozoic Lomagundi Event. *Earth and Planetary Science Letters* 486, 70–83.

Pasquier V., Sansjofre P., Rabineau M., Revillon S., Houghton J., and Fike D.A. (2017) Pyrite sulfur isotopes reveal glacial−interglacial environmental changes: *Proceedings of the National Academy of Sciences* 114, 5941–5945.

Penniston-Dorland S.C., Mathez E.A., Wing B.A., Farquhar J., and Kinnaird J.A. (2012) Multiple sulfur isotope evidence for surface-derived sulfur in the Bushveld Complex. *Earth and Planetary Science Letters* 337, 236–242.

Poulton S. W. and Canfield D. E. (2005) Development of a sequential extraction procedure for iron: implications for iron partitioning in continentally derived particulates. *Chemical Geology* 214, 209–221.

Poulton S. W. and Canfield D. E. (2011) Ferruginous Conditions: A Dominant Feature of the Ocean through Earth's History. *Elements* 7, 107–112.

Poulton S. W. and Raiswell R. (2002) The low-temperature geochemical cycle of iron: From continental fluxes to marine sediment deposition. *American Journal of Science* 302, 774–805.

Priyatkina N., Khudoley A. K., Ustinov V. N. and Kullerud K. (2014) 1.92 Ga kimberlitic rocks from Kimozero, NW Russia: Their geochemistry, tectonic setting and unusual field occurrence. *Precambrian Research* 249, 162–179.

Puchtel I. S., Arndt N. T., Hofmann A. W., Haase K. M., Kroner A., Kulikov V. S., Kulikova V. V., Garbe-Schonberg C. D. and Nemchin A. A. (1998) Petrology of mafic lavas within the Onega plateau, central Karelia: evidence for 2.0 Ga plume-related continental crustal growth in the Baltic Shield. *Contributions to Mineralogy and Petrology* 130, 134–153.

Puchtel I. S., Brugmann G. E. and Hofmann A. W. (1999) Precise Re-Os mineral isochron and Pb-Nd-Os isotope systematics of a mafic-ultramafic sill in the 2.0 Ga Onega plateau (Baltic Shield). *Earth and Planetary Science Letters* 170, 447–461.

Qu Y., Crne A. E., Lepland A. and Van Zuilen M. A. (2012) Methanotrophy in a Paleoproterozoic oil field ecosystem, Zaonega Formation, Karelia, Russia. *Geobiology* 10, 467–478.

Qu Y., Lepland A., van Zuilen M.A., Whitehouse M., Črne A.E., Fallick A.E. (2018) Sample-scale carbon isotopic variability and diverse biomass in the Paleoproterozoic Zaonega Formation, Russia. *Precambrian Research* 315, 222–231.

Raiswell R., Canfield D. E. and Berner R. A. (1994) A Comparison of Iron Extraction Methods for the Determination of Degree of Pyritisation and the Recognition of Iron-Limited Pyrite Formation. *Chemical Geology* 111, 101–110.

Raiswell, R., Reinhard, C.T., Derkowski, A., Owens, J., Bottrell, S.H, Anbar, A.D., Lyons, T.W. (2011) Formation of syngenetic and early diagenetic iron minerals in the late Archean Mt. McRae Shale, Hamersley Basin, Australia: New insights on the patterns, controls and paleoenvironmental implications of authigenic mineral formation. *Geochimica et Cosmochimica Acta* 75, 1072–1082.

Rees C. E., Jenkins W. J. and Monster J. (1978) The sulphur isotope geochemistry of ocean water sulphate. *Geochimica et Cosmochimica Acta* 42, 377–381.

Reuschel M., Melezhik V. A., Whitehouse M. J., Lepland A., Fallick A. E. and Strauss H. (2012) Isotopic evidence for a sizeable seawater sulfate reservoir at 2.1 Ga. *Precambrian Research* 192-95, 78–88.

Ripley E.M., Wernette B.W., Ayre A., Li C., Smith J.M., Underwood B.S., and Keays R.R. (2017) Multiple S isotope studies of the Stillwater Complex and country rocks: An assessment of the role of crustal S in the origin of PGE enrichment found in the J-M Reef and related rocks. *Geochimica et Cosmochimica Acta* 214, 226–245.

Schröder S., Bekker A., Beukes N. J. Strauss, H. van Niekerk, H. S. (2008) Rise in seawater sulphate concentration associated with the Paleoproterozoic positive carbon isotope excursion: evidence from sulphate evaporites in the similar to 2.2–2.1 Gyr shallow-

marine Lucknow Formation, South Africa (vol 20, pg 108 2008). *Terra Nova* 20, 252–252.

Scott C., Wing B. A., Bekker A., Planavsky N. J., Medvedev P., Bates S. M., Yun M. and Lyons T. W. (2014) Pyrite multiple-sulfur isotope evidence for rapid expansion and contraction of the early Paleoproterozoic seawater sulfate reservoir. *Earth and Planetary Science Letters* 389, 95–104.

Seal R. R. (2006) Sulfur isotope geochemistry of sulfide minerals. *Reviews in Mineralogy and Geochemistry* 61, 633–677.

Shatsky G. V. (1990) Isotope composition of sulphides from the Zazhogino shungite deposit. *Lithology and Mineral Deposits* 1, 20–28 (in Russian).

Sim M. S., Bosak T. and Ono S. (2011) Large Sulfur Isotope Fractionation Does Not Require Disproportionation. *Science* 333, 74–77.

Slotznick S.P., Eiler J.M., and Fischer W.W. (2018) The effects of metamorphism on iron mineralogy and the iron speciation redox proxy. *Geochimica et Cosmochimica Acta* 224, 96–115.

Stepanova A. V., Samsonov A. V. and Larionov A. N. (2014) The final episode of middle Proterozoic magmatism in the Onega structure: data on trans-Onega dolerites. *Proceedings of the Karelian Research Centre of the Russian Academy of Sciences* 1, 3–16 (in Russian).

Strauss H., Melezhik V. A., Lepland A., Fallick A. E., Hanski E. J., Filippov M. M., Deines Y. E., Illing C. J., Črne A. E. and Brasier A. T. (2013) Enhanced accumula-tion of organic matter: The Shunga event, in: Melezhik V. A., Kump L. R., Fallick A. E., Strauss H., Hanski E., Prave A. R., Lepland A. (Eds.), *Reading the Archive of Earth's Oxygenation: Volume 3: Global Events and the Fennoscandian Arctic Russia - Drilling Early Earth Project*. Springer, Berlin Heidelberg, 1195–1273.

Tostevin R., Turchyn A. V., Farquhar J., Johnston D. T., Eldridge D. L., Bishop J. K. B. and McIlvin M. (2014) Multiple sulfur isotope constraints on the modern sulfur cycle. *Earth and Planetary Siencec Letters* 396, 14–21.

Wagner T. and Boyce A. J. (2006) Pyrite metamorphism in the Devonian Hunsruck Slate of Germany: Insights from laser microprobe sulfur isotope analysis and thermodynamic modeling. *American Journal of Science* 306, 525–552.

Zaback D. A., Pratt L. M., and Hayes J. M. (1993) Transport and reduction of sulfate and immobilization of sulfide in marine black shales. *Geology* 21, 141–144.

Zerkle A. L., Farquhar J., Johnston D. T., Cox R. P. and Canfield D. E. (2009) Fractionation of multiple sulfur isotopes during phototrophic oxidation of sulfide and elemental sulfur by a green sulfur bacterium. *Geochimica et Cosmochimica Acta* 73, 291–306.

Zerkle A. L., Jones D. S., Farquhar J. and Macalady J. L. (2016) Sulfur isotope values in the sulfidic Frasassi cave system, central Italy: A case study of a chemolithotrophic S-based ecosystem. *Geochimica et Cosmochimica Acta* 173, 373–386.

Figure captions

Figure 1. A. Simplified geological map of the Onega basin, NW Russia. Circles show locations of the OnZap 1 and 3 holes, FAR-DEEP holes 12AB, 13A, Onega Parametric Hole (OPH) and the C-175 and C-5190 holes. Inset map shows location of the Onega basin and occurrence of Paleoproterozoic rocks (black) across the eastern Fennoscandian Shield. B. Simplified geological map of the Zaonega Formation (after Melezhik et al., 2013a) near locations of OnZap 1 and 3 holes and FAR-DEEP hole 13A.

Figure 2. Representative images of the OnZap cores. A. Fine-grained laminated mudstone with pyrite concretions and layers (11.8 m depth). B. Laminated fine-grained dolostone (13.4 m depth). C. Finely parallel-laminated to ripple cross-laminated grey mudstone (19.38 m depth). D. Laminated organic-rich mudstone with soft-sediment deformation, quartz and pyrobitumen veining (63.4 m depth). E. Silicified organic-rich mudstone displaying deformation, intense veining and secondary pyrite (76.5 m depth). The width of all the images is 7 cm.

Figure 3. Scanning Electron Microscopy (SEM) images of different textural types of pyrite. A. Organic-rich mudstone containing ellipsoidal clusters of fine pyrite crystals at 53.78 m depth; early diagenetic origin is indicated by the deflection of laminae around the clusters. B. Organic-rich mudstone with abundant fine pyrite crystals at 56.66 m depth. C. Close-up of fine-grained pyrite in image 3B containing inclusions of surrounding material in the central parts of the

crystals. D. SEM EDS element composite map of large anhedral pyrite in a calcareous mudstone that appears texturally co-genetic with calcite at 26.8 m depth.

Figure 4. Generalised lithostratigraphic profile of the OnZap section divided into Units A to C (see text for details) and XRD-derived distributions of select mineral phases. The two OnZap cores are correlated using the base of a dolomite-chert unit occurring at 53 m in OnZap1 and at 10.8 m in OnZap3. Horizontal grey-shaded bars show intervals with evidence for secondary alteration. Grey and black data points denote samples from OnZap 1 and OnZap 3, respectively.

Figure 5. Generalised lithostratigraphic profile of the OnZap section divided into Units A to C (see text for details) plotted alongside selected components (TOC; TS; Fe_2O_3; SiO_2; Al_2O_3 and K_2O). The two OnZap cores are correlated using the base of a dolomite-chert unit occurring at 53 m in OnZap1 and at 10.8 m in OnZap3. Horizontal grey-shaded bars show intervals with evidence for secondary alteration. Grey and black data points denote samples from OnZap1 and OnZap3, respectively.

Figure 6. Generalised lithostratigraphic profile of the OnZap section divided into Units A to C (see text for details) plotted alongside carbon and sulphur isotope data and XRD-derived iron distribution data. The two OnZap cores are correlated using the base of a dolomite-chert unit occurring at 53 m in OnZap1 and at 10.8 m in OnZap3. Horizontal grey-shaded areas show intervals with evidence for secondary alteration. Grey and black data points denote samples from OnZap 1 and OnZap 3, respectively, whereas blue dots represent AVS results. Errors for the $\delta^{13}C_{org}$ and $\delta^{34}S$ are encompassed within the data points whereas the grey-shaded envelope illustrates the 1σ estimates of the analytical uncertainty for the $\Delta^{33}S$ (0.015‰) and $\Delta^{36}S$ (0.2‰) data.

Figure 7. Sulphur (TS) and iron ($Fe_{T\text{-}OES}$) concentrations for the entire OnZap section. Black circles are derived from Unit A, grey circles from Unit B and orange circles from Unit C. Errors are encompassed within each data point.

Figure 8. Triple-isotope plot of the pyrite sulphur isotope data for the entire OnZap section. Black circles are derived from Unit A, grey circles from Unit B and orange circles from Unit C. Uncertainties in the $\Delta^{33}S$ values (0.015‰) are illustrated in grey, whereas the uncertainty in $\delta^{34}S$ values are encompassed within each data point.

Figure 9. Quadruple-isotope plot of the pyrite sulphur isotope data for the entire OnZap section. Black circles are derived from Unit A and orange circles are from Units B and C. The dashed

lines are regressions through the datasets derived from Unit A (-7.66; black) and Units B and C (-4.10; orange). The analytical uncertainties (1σ) in both $\Delta^{33}S$ (0.015‰) and $\Delta^{36}S$ (0.2‰) are illustrated in grey.

Highlights:

- Zaonega Formation $\Delta^{33}S$-$\delta^{34}S$ data track basin-specific rather than global processes.
- Opposing $\Delta^{33}S$-$\delta^{34}S$ relationship relates to rapid microbial sulphate reduction.
- Positive $\delta^{34}S$ excursions reflect partial basinal restriction.

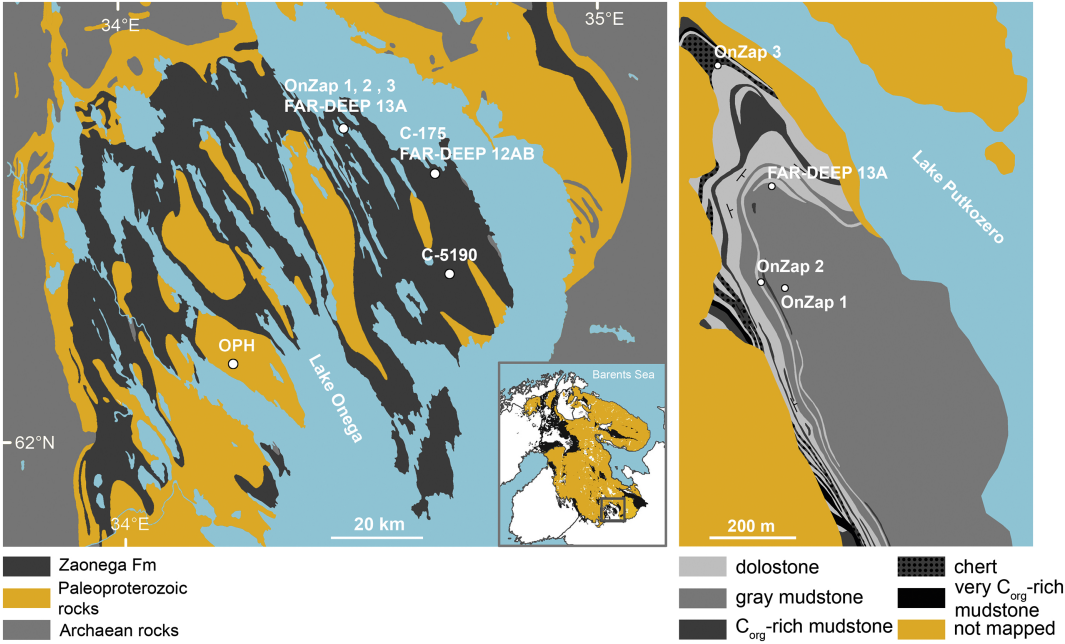
34°E
35°E
OnZap 1, 2 , 3
FAR-DEEP 13A
C-175
FAR-DEEP 12AB
C-5190
OPH
Lake Onega
62°N
34°E
20 km
Barents Sea
OnZap 3
FAR-DEEP 13A
Lake Putkozero
OnZap 2
OnZap 1
200 m
Zaonega Fm
Paleoproterozoic rocks
Archaean rocks
dolostone
gray mudstone
C_{org}-rich mudstone
chert
very C_{org}-rich mudstone
not mapped

Figure 1

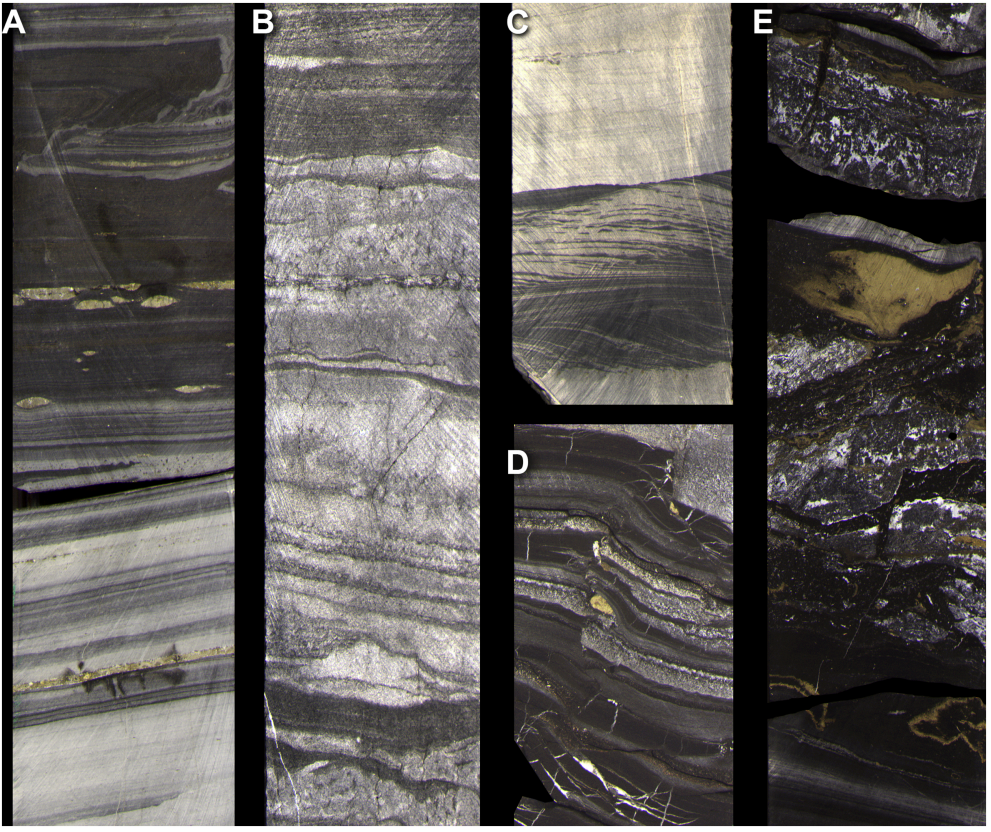

Figure 2

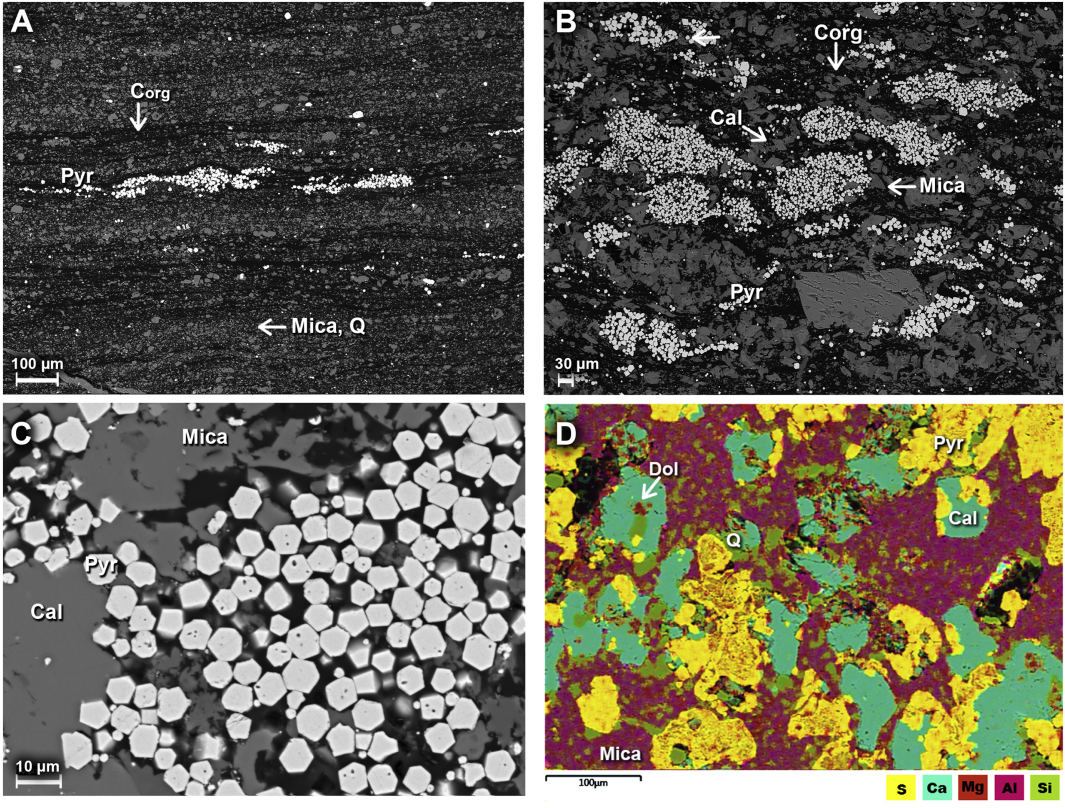
A
Corg
Pyr
Mica, Q
100 µm
B
Corg
Cal
Mica
Pyr
30 µm
C
Mica
Pyr
Cal
10 µm
D
Dol
Pyr
Cal
Q
Mica
100µm
S
Ca
Mg
Al
Si

Figure 3

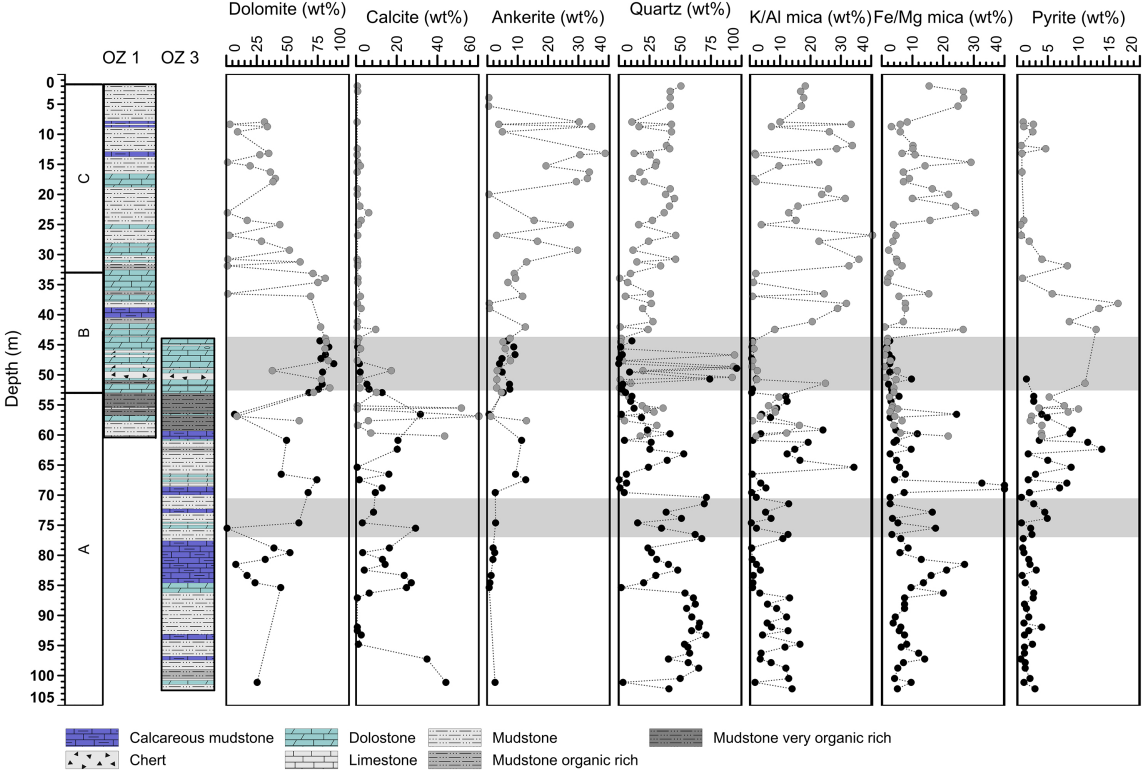
Dolomite (wt%)
Calcite (wt%)
Ankerite (wt%)
Quartz (wt%)
K/Al mica (wt%)
Fe/Mg mica (wt%)
Pyrite (wt%)
OZ 1
OZ 3
Depth (m)
A
B
C
Calcareous mudstone
Chert
Dolostone
Limestone
Mudstone
Mudstone organic rich
Mudstone very organic rich

Figure 4

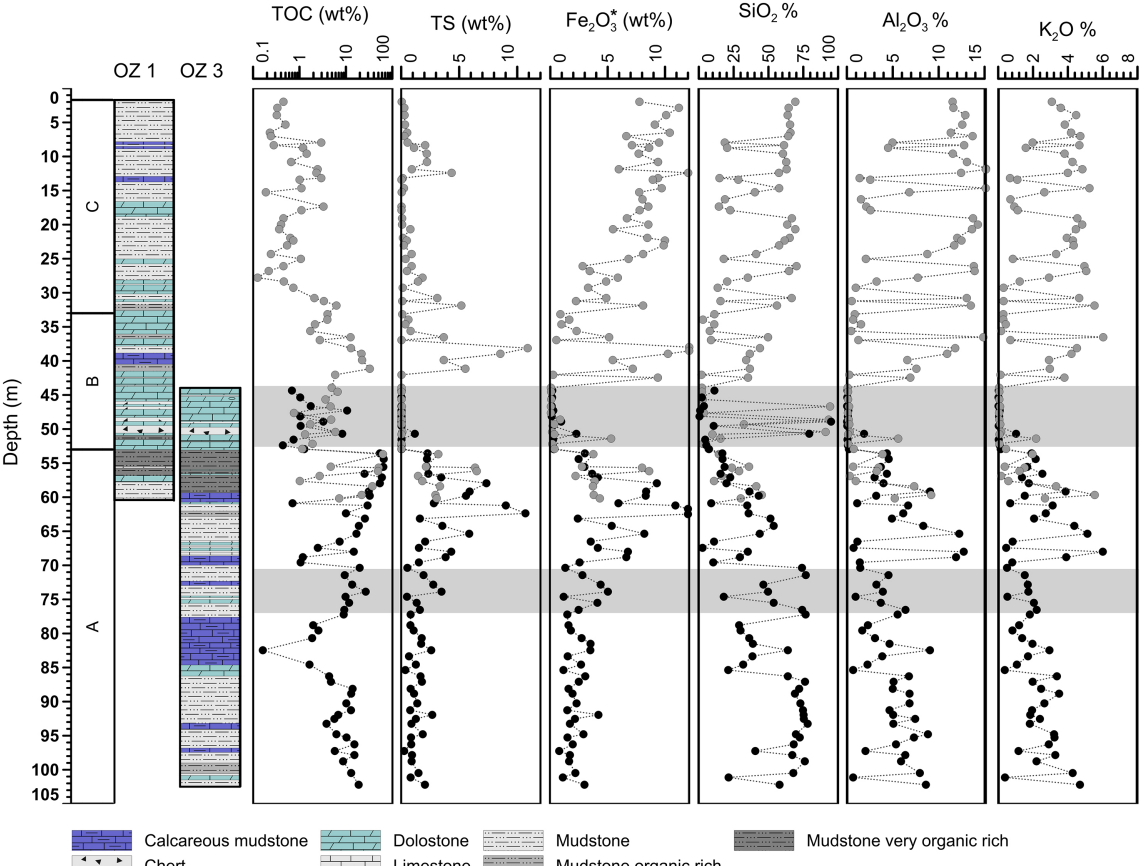
TOC (wt%)
TS (wt%)
$Fe_2O_3^*$ (wt%)
SiO_2 %
Al_2O_3 %
K_2O %
OZ 1
OZ 3
Depth (m)
A
B
C
Calcareous mudstone
Chert
Dolostone
Limestone
Mudstone
Mudstone organic rich
Mudstone very organic rich

Figure 5

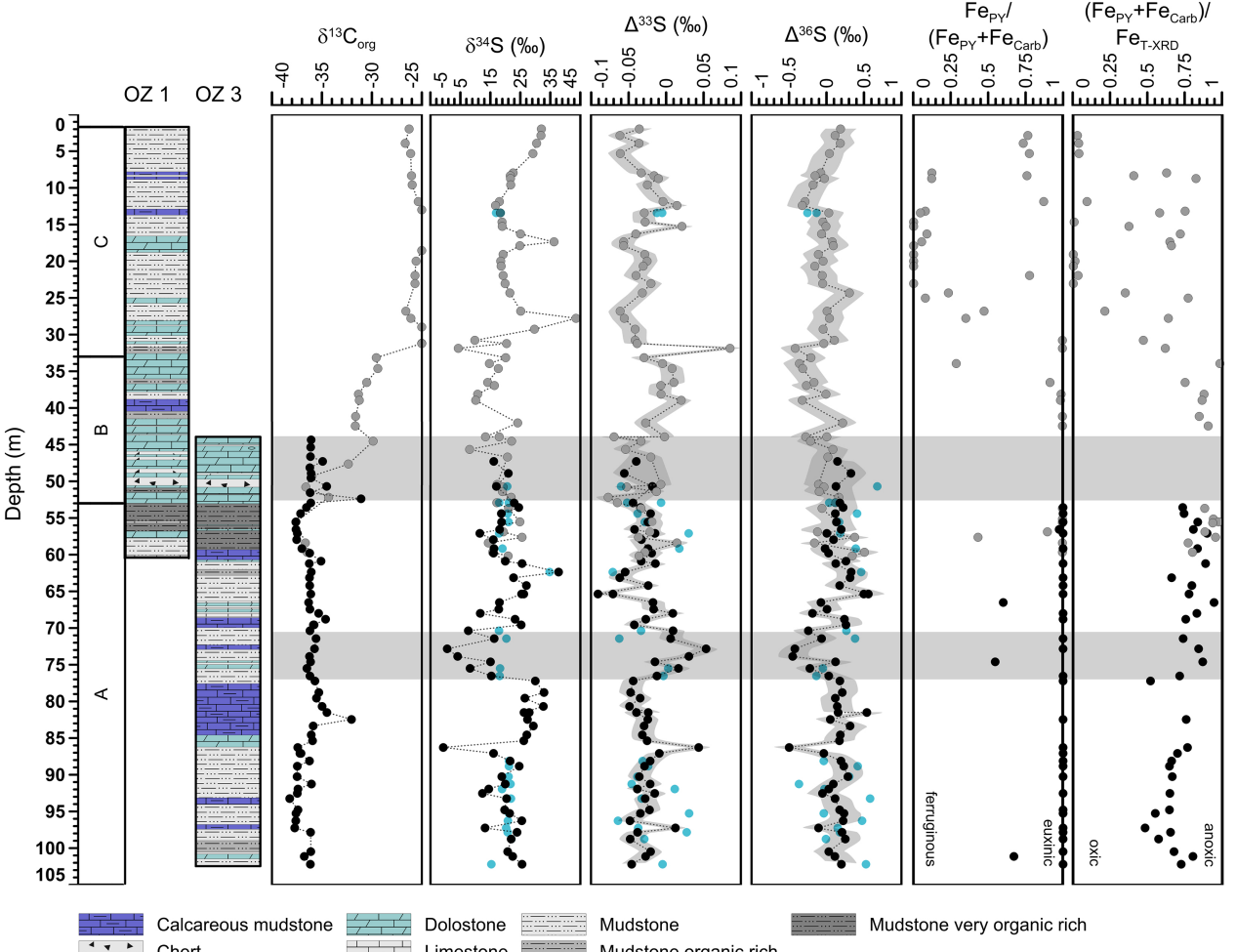
δ13Corg
δ34S (‰)
Δ33S (‰)
Δ36S (‰)
FePY/ (FePY+FeCarb)
(FePY+FeCarb)/ FeT-XRD
OZ 1
OZ 3
Depth (m)
A
B
C
ferruginous
euxinic
oxic
anoxic
Calcareous mudstone
Chert
Dolostone
Limestone
Mudstone
Mudstone organic rich
Mudstone very organic rich

Figure 6

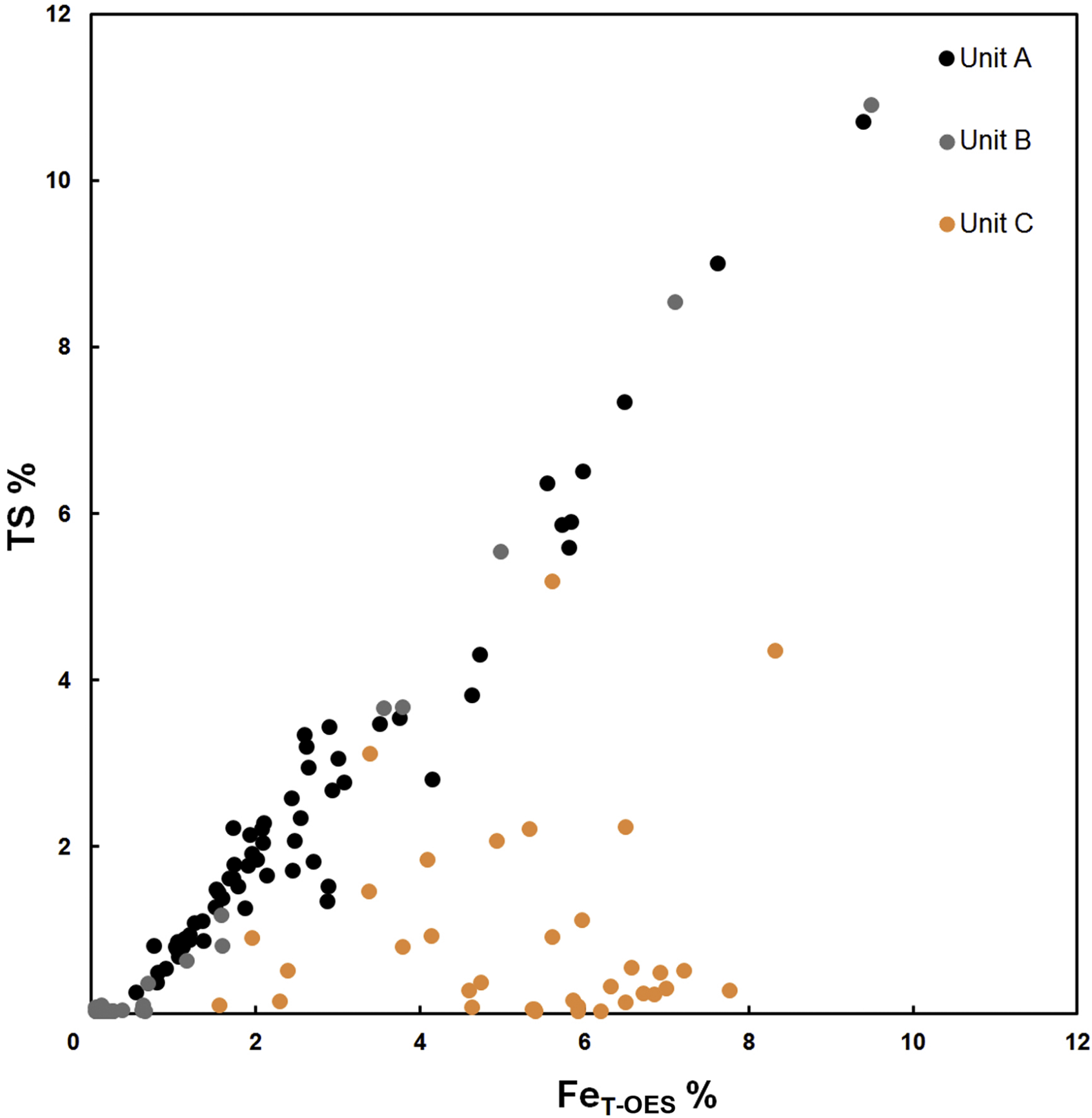

Figure 7

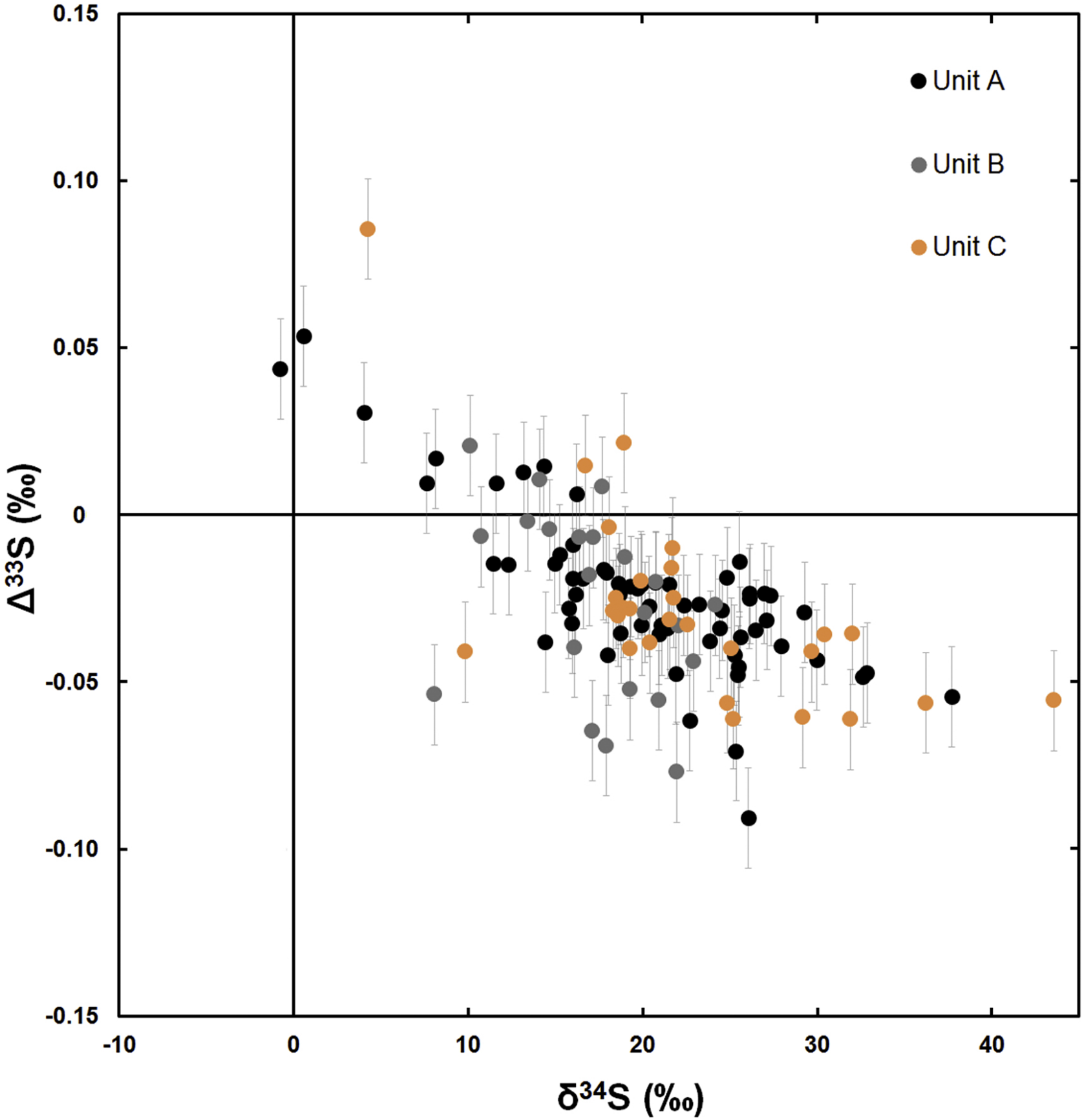
Unit A
Unit B
Unit C
0.15
0.10
0.05
0
-0.05
-0.10
-0.15
Δ33S (‰)
-10
0
10
20
30
40
δ34S (‰)

Figure 8

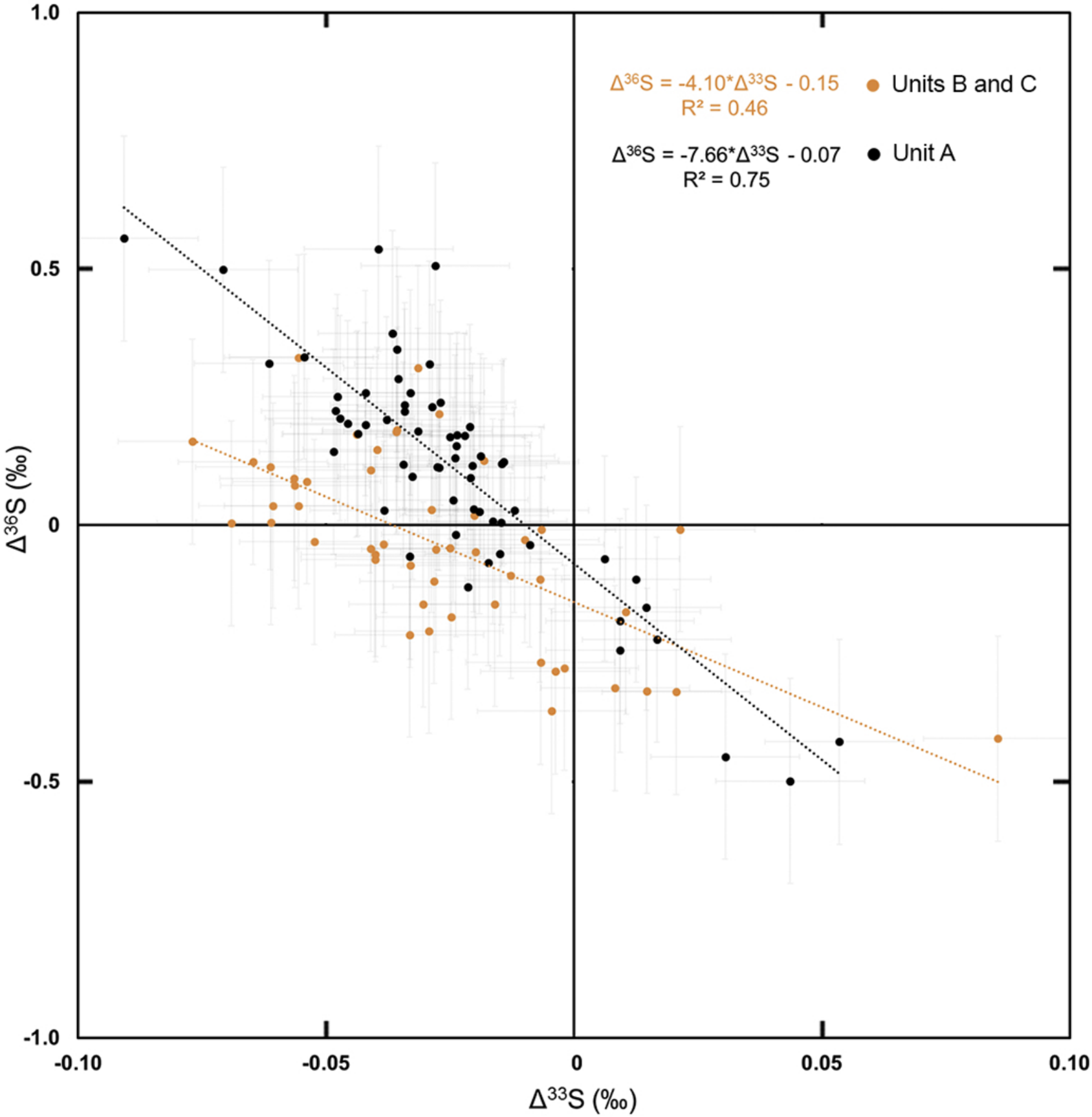
1.0
0.5
0
-0.5
-1.0
-0.10
-0.05
0
0.05
0.10
Δ36S (‰)
Δ33S (‰)
Δ36S = -4.10*Δ33S - 0.15
R² = 0.46
Units B and C
Δ36S = -7.66*Δ33S - 0.07
R² = 0.75
Unit A

Figure 9

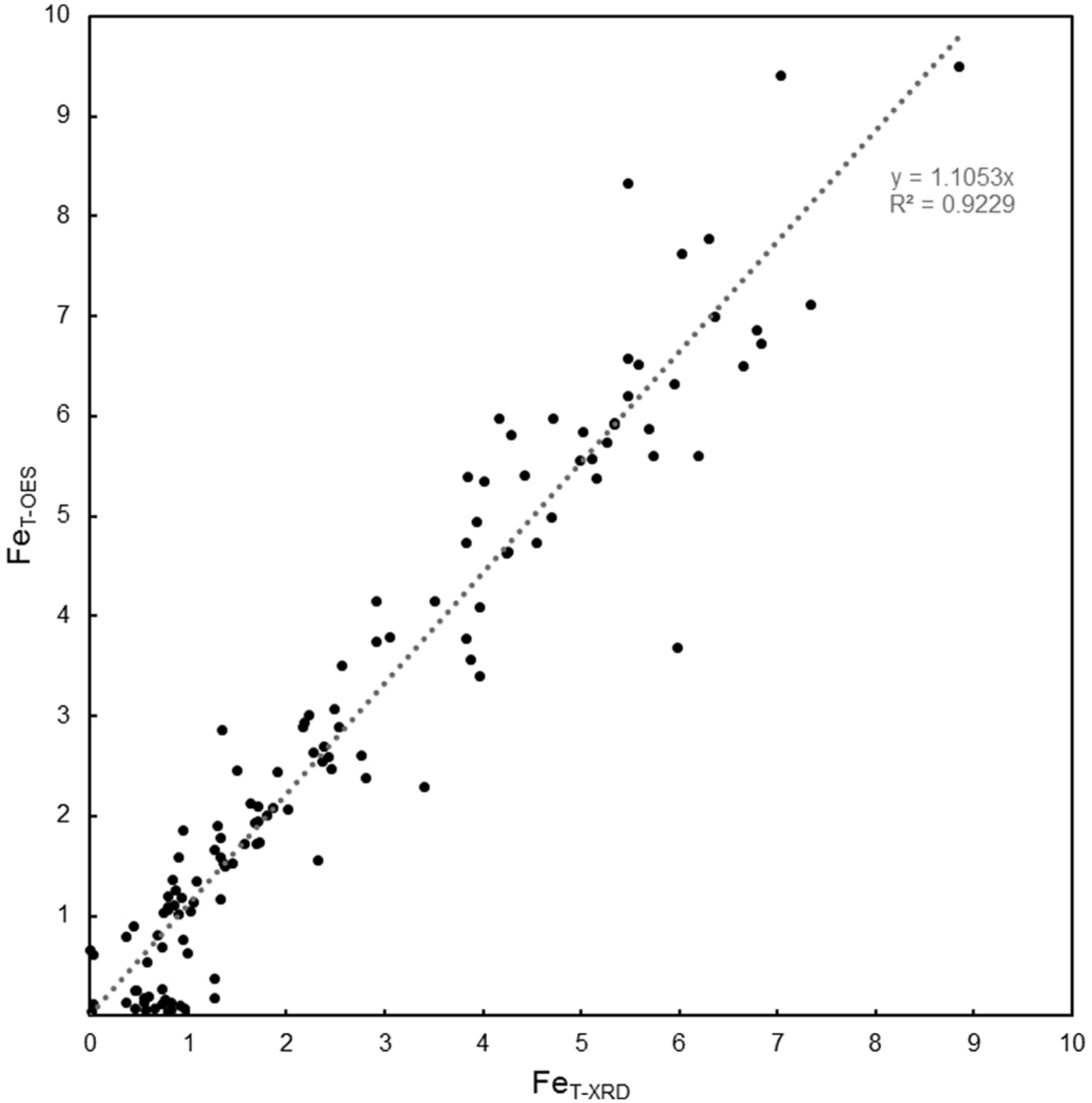

Figure 10